

Einstein Probe discovery of EP J171159.4–333253: an eclipsing neutron star low-mass X-ray binary with clocked bursts

Y. L. WANG ^{1, 2, 3, 4} F. COTI ZELATI ^{2, 3, 5} E. PARENT ^{2, 3} A. MARINO ^{2, 3, 6} N. REA ^{2, 3} V. S. DHILLON ^{7, 8}
 J. BLANCO-POZO, ^{2, 3} I. RIBAS ^{2, 3} S. P. LITTLEFAIR ⁷ Z. H. YANG ^{9, 4} G. B. ZHANG ^{10, 11} S. GUILLOT ¹²
 K. R. NI ¹³ J. H. WU ¹⁴ A. PATRUNO ^{2, 3} Y. CAVECHI ^{15, 16} G. ILLIANO ⁵ A. PAPITTO ¹⁷
 F. AMBROSINO ¹⁷ B. F. LIU ^{1, 4} H. Q. CHENG ¹ H. FENG ⁹ J. W. HU ¹ C. C. JIN ^{1, 4, 18} H. SUN ¹
 L. TAO ⁹ Y. J. XU, ⁹ H. N. YANG ¹ W. YUAN, ^{1, 4} AND Q. C. ZHAO ^{9, 4}

¹National Astronomical Observatories, Chinese Academy of Sciences, 20A Datun Road, Beijing 100101, China

²Institute of Space Sciences (ICE, CSIC), Campus UAB, Carrer de Can Magrans s/n, Barcelona, E-08193, Spain

³Institut d'Estudis Espacials de Catalunya (IEEC), Carrer Gran Capità 2–4, Barcelona, E-08034, Spain

⁴School of Astronomy and Space Science, University of Chinese Academy of Sciences, 19A Yuquan Road, Beijing 100049, China

⁵INAF–Osservatorio Astronomico di Brera, Via Bianchi 46, I-23807 Merate (LC), Italy

⁶INAF, Istituto di Astrofisica Spaziale e Fisica Cosmica, Via U. La Malfa 153, I-90146 Palermo, Italy

⁷Astrophysics Research Cluster, School of Mathematical & Physical Sciences, University of Sheffield, Sheffield S3 7RH, UK

⁸Instituto de Astrofísica de Canarias, E-38205 La Laguna, Tenerife, Spain

⁹Key Laboratory of Particle Astrophysics, Institute of High Energy Physics, Chinese Academy of Sciences, Beijing 100049, China

¹⁰Yunnan Observatories, Chinese Academy of Sciences, Kunming 650216, China

¹¹Key Laboratory for the Structure and Evolution of Celestial Objects, Chinese Academy of Sciences, Kunming 650216, China

¹²Institut de Recherche en Astrophysique et Planétologie, UPS-OMP, CNRS, CNES, 9 avenue du Colonel Roche, BP 44346, Toulouse Cedex 4, 31028, France

¹³Institute of Astrophysics, Central China Normal University, Wuhan 430079, China

¹⁴Department of Astronomy, Guangzhou University, Guangzhou 510006, China

¹⁵Departament de Física, EEBE, Universitat Politècnica de Catalunya, Av. Eduard Maristany 16, 08019 Barcelona, Spain

¹⁶Center for Nuclear Astrophysics across Messengers (CeNAM), 640 S Shaw Lane, East Lansing, MI 48824, USA

¹⁷INAF–Osservatorio Astronomico di Roma, Via Frascati 33, I-00078 Monte Porzio Catone (RM), Italy

¹⁸Institute for Frontier in Astronomy and Astrophysics, Beijing Normal University, Beijing 102206, China

Submitted to ApJ

ABSTRACT

EP J171159.4–333253 is a new neutron-star low-mass X-ray binary discovered in outburst by the *Einstein Probe* (EP) on 2025 June 23, exhibiting clocked type-I X-ray bursts, eclipses and dips. In this paper, we report on the results of the X-ray spectral and timing analyses for EP J171159.4–333253 using data collected by EP and *NuSTAR* during the first 21 days of the outburst. The X-ray burst recurrence time can be characterized over a subset of nine bursts spanning 1.6 days around the *NuSTAR* observation, and the result is $t_{\text{rec}} = 8196 \pm 177$ s with indications of a possible decreasing trend. From the X-ray eclipse events, the binary orbital period and the eclipse duration are estimated to be $P_{\text{orb}} = 6.48301 \pm 0.00003$ hr and $D_{\star, X} = 1245.5^{+6.9}_{-6.5}$ s, respectively. These enable an estimate of the mass and radius of the companion star and the binary inclination, which are $M_2 \approx 0.6 - 0.8 M_{\odot}$, $R_2 \approx 0.7 - 0.8 R_{\odot}$ and $i \approx 73 - 75^\circ$, respectively. We also report on joint ULTRACAM and EP observations on 2025 July 21–22, detecting the source optical counterpart and covering an eclipse in both X-ray and optical bands. The optical eclipse is wavelength-dependent and broader than in X-rays, indicating that part of the optical emission arises from an extended region in the accretion flow. Despite a moderate variation in the source flux, the properties of the persistent X-ray emission are typical of a hard spectral state. We further evaluated the ratio of the accretion energy to the thermonuclear energy to be 120–130, implying helium bursts with the accreted hydrogen being depleted in-between bursts.

Corresponding author: Yilong Wang
 Email: wangyilong@nao.cas.cn

Keywords: Accretion (14) — Eclipses (442) — Neutron stars (1108) — X-ray bursters (1813) — X-ray transient sources (1852)

1. INTRODUCTION

Low-mass X-ray binaries (LMXBs) are binary systems composed of a compact stellar object, either a black hole (BH) or a neutron star (NS), and a companion star typically with a mass comparable to or less than the solar mass (for a recent review, see [A. Bahramian & N. Degenaar 2022](#)). In NS-LMXBs, the matter accreted on top of the NS surface can sometimes undergo thermonuclear runaways and produce explosions, known as type-I X-ray bursts ([D. K. Galloway & L. Keek 2021](#)). These phenomena require the accreting compact object to possess a solid surface, making type-I X-ray bursts exclusive to NS-LMXBs and thus a clear signature of an NS accretor. Type-I X-ray bursts are usually observed to repeat at variable intervals, depending on the accretion rate of the system as well as the chemical composition of the accreted matter. Among more than one hundred previously known bursters ([D. K. Galloway et al. 2020](#)), only seven sources are known to have shown bursts that repeat quasi-periodically, which are referred to as *clocked* bursters: GS 1826–24 (the prototype; e.g. [P. Ubertini et al. 1999](#)), KS 1731–260 ([R. Cornelisse et al. 2003](#)), GS 0836–429 ([E. Aranzana et al. 2016](#)), IGR J17480–2446 ([S. Motta et al. 2011; M. Chakraborty et al. 2011](#)), MAXI J1816–195 ([P. Bult et al. 2022; P. J. Wang et al. 2024](#)), 1RXS J180408.9–342058 ([A. Marino et al. 2019; M. Fiocchi et al. 2019](#)) and SRGA J144459.2–60420 ([M. Ng et al. 2024; S. V. Molkov et al. 2024; A. Dohi et al. 2025; A. Papitto et al. 2025](#)).

In this paper, we report on the discovery of a new clocked burster, EP J171159.4–333253 (hereafter EP J1711–3332). EP J1711–3332 was first detected by the Wide-field X-ray Telescope (WXT) on board the *Einstein Probe* (EP) mission ([W. Yuan et al. 2022, 2025](#)) in one observation performed on 2025 June 23, and therefore was initially designated as EP250623a ([K. R. Ni et al. 2025](#)). However, stacking of WXT data showed that a weak signal from the source location could already be detected at least on June 21. Then, on June 25, a target-of-opportunity (ToO) observation at the WXT position was performed with the Follow-up X-ray Telescope (FXT) on board EP. An uncatalogued X-ray source was detected at R. A. (J2000) = $17^{\text{h}}11^{\text{m}}59.4^{\text{s}}$, Dec. (J2000) = $-33^{\circ}32'53''$, with an uncertainty of $10''$ in radius (90% confidence level, statistical and systematic), giving the source a final designation of EP J171159.4–333253 ([J. Wu et al. 2025](#)). The FXT light curve, apart from the persistent emission, showed a short burst lasting ~ 100 s and a low-count-rate period (later identified as a dip event), which, together with the low Galactic latitude of EP J1711–3332, led

to the tentative identification of the source as an eclipsing NS-LMXB. A *Nuclear Spectroscopic Telescope Array* (*NuSTAR*) follow-up observation was performed on 2025 June 27. Seven bursts with quasi-periodic recurrence time of ~ 8200 s were detected ([A. Marino et al. 2025](#)), suggesting that EP J1711–3332 is a clocked burster.

A radio follow-up observation performed with *MeerKAT* on 2025 June 30 revealed a counterpart within the FXT position error, with a 1.3-GHz flux density of $108 \pm 20 \mu\text{Jy}$ ([F. J. Cowie et al. 2025](#)). In the optical band, on 2025 June 28, a ToO observation with the Visible Telescope (VT) on board the *Space Variable Objects Monitor* (SVOM) detected a candidate optical counterpart with magnitudes of ~ 18.5 mag and ~ 20.0 mag in the VT-Red and VT-Blue bands, respectively ([S. Guillot et al. 2025](#)). However, the source was not detected in two observations performed respectively with the 0.4-m *Super Light Telescope* (SLT) and the 0.5-m *Robotic Imager For Transients* (RIFT) at Lulin Observatory on 2025 June 27 and July 3, which gave 3σ upper limits of 18.8 mag with the rp filter of SLT and 19.0 mag with the white filter of RIFT ([A. K. H. Kong et al. 2025](#)). On 2025 July 21, we confirmed the optical counterpart of EP J1711–3332 using the ULTRACAM camera mounted on the 3.5-m *New Technology Telescope* (NTT), as reported in this work.

This paper is structured as follows: in Section 2, we describe the X-ray and optical observations and the data reduction procedures. The results of our data analysis are presented in Section 3, and then discussed in Section 4. Finally, we summarize in Section 5.

2. OBSERVATIONS AND DATA REDUCTION

Our main dataset includes observations obtained over the first 21 days of the outburst with the following X-ray telescopes: WXT and FXT on board EP and *NuSTAR* (see Table A1 for details). Photon arrival times recorded by the different instruments were corrected to the Solar System barycenter using the JPL DE430 ephemeris and the source position determined from *MeerKAT* observations: R. A. = $17^{\text{h}}11^{\text{m}}59.31^{\text{s}}$, Dec. = $-33^{\circ}32'52.5''$ (J2000.0; [F. J. Cowie et al. 2025](#)).

Additionally, we present the results of an optical observation performed on 2025 July 21–22 by ULTRACAM, and partial results of a simultaneous X-ray observation by EP/FXT. A detailed analysis of this X-ray observation will be presented in a companion paper (Yang et al., in prep.).

2.1. Einstein Probe

The WXT on board EP detected X-ray emission from the position of EP J1711–3332 in a snapshot beginning on 2025 June 23 at 12:37:24 UTC. From that moment on

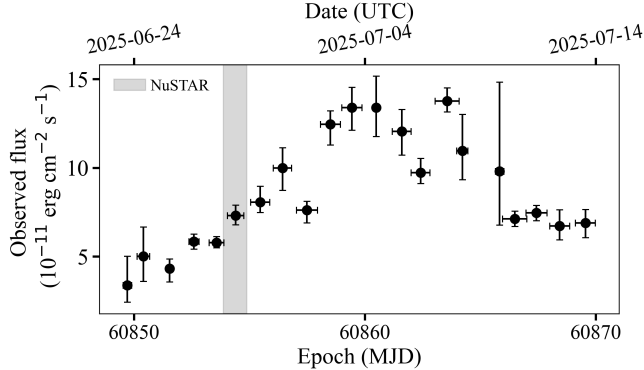


Figure 1. X-ray light curve of EP J1711–3332 extracted from EP/WXT data collected during the first 21 days of the outburst. Observed fluxes refer to the 0.5–4 keV energy range and were obtained by combining data from snapshots taken on the same day. The shaded gray area marks the epoch of the *NuSTAR* observation.

and until July 13, the source was detected by WXT for a total of 184 times, with individual snapshot exposures ranging from 0.4 to 9.3 ks and a total exposure time of ~ 0.5 Ms. Figure 1 presents the light curve, binned approximately on a daily timescale, derived by combining all spectral data acquired each day and fitting the resulting spectra with an absorbed power-law model. In the fits, the value for the absorption column density was held fixed to the value obtained from the broadband spectral analysis (Section 3.4.1), whereas the power-law photon index, Γ , was allowed to vary.

The first follow-up observation with FXT on board EP was performed on 2025 June 25 at 14:09:08 UTC, two days after the WXT detection. In this observation, an X-ray burst and part of an eclipse event were detected, which motivated a daily monitoring program with FXT. In this work, we analyzed the dataset of the first 22 EP/FXT observations collected over 21 days following the onset of the outburst. The remaining ~ 30 observations will be discussed in a companion paper (Yang et al., in prep.). The data were reduced with the `fxtchain` tool available within the FXT Data Analysis Software Package (FXTDAS). Further filtering of the data was performed with `Xselect`. EP/FXT consists of two identical modules, FXT-A and FXT-B. During the observation, the two modules can be set in different science modes, including Partial Window mode (PW, with a time resolution of 2 ms), Full Frame mode (FF, with a time resolution of 50 ms) and Timing mode (TM, with a time resolution of 23.6 μ s). For PW and FF data, a circular source region with a radius of 60'' and an annular background region with inner and outer radii of 120'' and 240'' were adopted. Moreover, for FF data the inner 10'' region around the source position was excluded, in order to mitigate the pile-up effect. For TM data, box regions ($180'' \times 60''$) aligned with the roll angle of the satellite during each observation were used for both

source and background extractions, with the center of the background region shifted from the source location by 360''.

2.2. NuSTAR

NuSTAR is a hard X-ray observatory consisting of two Wolter-I telescopes, focusing X-rays onto two Focal Plane Modules (FPM), labeled A and B (F. A. Harrison et al. 2013). Operating in the 3–79 keV band, it provides high-sensitivity timing measurements with a time resolution of about 2 μ s. A *NuSTAR* observation targeting the source was carried out on 2025 June 27, for a total on-source exposure of 46.7 ks. We reduced the data from both FPM detectors using standard tools within the *NuSTARDAS* package. The source region was extracted using a circular region of 100'' radius centered at the coordinates of the source. To account for any background non-uniformity on the detector, we extracted the background spectra using four circles of $\sim 50''$ radii located away from the source, at different places in the field of view. We extracted the light curves with `Xselect` and inspected them in search for type-I X-ray bursts, eclipses and/or dips. In order to isolate the persistent emission, we ran *NuPRODUCTS* to extract spectra and light curves from an event file in which these phenomena had been filtered out. Additionally, separate *NuPRODUCTS* runs were performed on event files containing only the bursts.

2.3. ULTRACAM

On the night of 2025 July 21, we observed EP J1711–3332 simultaneously in *u*_{sgs} filters using the high-speed, triple-beam imager ULTRACAM (V. S. Dhillon et al. 2007) on the 3.5-m NTT at La Silla, Chile. We used the so-called Super SDSS filters in ULTRACAM, which are more top-hat in shape than the original SDSS filter set and have significantly higher throughputs, particularly in the *u*_S and *g*_S bands (see V. S. Dhillon et al. 2021). A total of 785 frames were obtained, each of 10.0 s exposure time. The instrument was used in full-frame mode, no-clear mode, giving a dead time of 0.024 s between each frame, where each ULTRACAM frame is GPS time-stamped to a relative (i.e. frame-to-frame) accuracy of 50 μ s and an absolute accuracy of 1 ms (V. S. Dhillon et al. 2007). The source was too faint to detect in the *u*_S-band frames and so will not be discussed further here.

The ULTRACAM data were reduced using the HiPERCAM data reduction pipeline (V. S. Dhillon et al. 2021). All frames were debiased and then flat-fielded, the latter using the median of twilight-sky frames taken with the telescope spiralling. Due to the crowded field, we used point-spread function (PSF) photometry to extract the counts from EP J1711–3332 and a number of comparison stars in the same field of view, the latter acting as the reference for the PSF fits, and providing corrections for transparency and extinction variations.

The comparison stars were also used for flux calibration via their magnitudes given in the SkyMapper Southern Sky Survey DR4 (C. A. Onken et al. 2024).

3. DATA ANALYSIS AND RESULTS

3.1. Timing analysis of the clocked bursts

3.1.1. Search for X-ray bursts

We searched for X-ray bursts by identifying statistically significant count rate excesses in the data. First, the cleaned, barycentered event data were binned into 2-s light curves. Assuming the background emission is dominated by Poisson noise, we computed the probability of observing the measured count rate or higher in each time interval, given the mean count rate of the observation. These Poisson tail probabilities were converted into Gaussian-equivalent significance values using the inverse complementary error function.

Burst candidates were defined as time intervals where the significance exceeded 3σ . The peak time of each burst was defined as the center of the time bin with the maximum sigma value. Burst start and end times were determined by tracking the rise and decay phases of the significance profile until the significance either ceased to decrease monotonically or fell below a 1σ threshold.

To maximize photon statistics, we performed the timing analysis of the bursts using the full energy band available for each dataset. We verified that the differences in the derived timing parameters when using the full band versus a fixed common energy range (e.g., 3–10 keV) are negligible as compared to the time resolution of the light curves.

In total, we identified 16 bursts, corresponding to 17 detections: ten in the EP/FXT data and seven in the *NuSTAR* observation (one of which was simultaneously detected by EP/FXT). Burst properties are listed in Table A2.

3.1.2. Burst recurrence time

To characterize the recurrence time of the bursts, t_{rec} , defined as the interval between consecutive burst onsets, we define burst times of arrival (TOAs) corresponding to the burst start times. TOA uncertainties were estimated from the flux rise duration, from the start time to the peak time.

First, we estimated t_{rec} using the seven detected bursts in the *NuSTAR* observation (see Figure 2) as this segment of the dataset exhibited the highest burst detection rate. Assuming a stable and periodic t_{rec} across the *NuSTAR* observation, we estimated the underlying periodicity by computing all pairwise TOA differences and identifying a common integer divisor. This yielded a period of approximately 8200 s, corresponding to a burst recurrence frequency ν_{rec} of ~ 0.122 mHz.

Next, we used the estimated ν_{rec} to attempt to derive a coherent timing solution across all 16 burst TOAs using the PINT pulsar timing software (J. Luo et al. 2021;

A. Susobhanan et al. 2024). We first fitted the data with a model in which ν_{rec} was the sole free parameter. We were unable to derive an acceptable solution — post-fit residuals spanned thousands of seconds, indicating the presence of intrinsic variation in the burst repetition frequency. We also found degeneracies in the inferred number of burst cycles between consecutive detections when the temporal gap exceeds approximately ten cycles. Introducing a first frequency derivative, $\dot{\nu}_{\text{rec}}$, as an additional free parameter did not produce a statistically significant improvement in the fit.

Lacking a coherent solution across all bursts, we opted to conservatively assess the timing variability of bursts by applying a timing model with ν_{rec} as the sole free parameter to pairs of consecutive bursts across the full TOA set. Measurements from TOA pairs yielding degenerate solutions were excluded from further analysis. Solutions for 8 of the 15 TOA pairs, covering all *NuSTAR* bursts, were obtained over a 1.6-day interval, from the EP/FXT burst on 2025-06-27 19:23:31 (UTC) to that on 2025-06-29 09:53:52 (UTC), corresponding to bursts No. 3–11 in Table A2. Best-fit t_{rec} values are shown in the left panel of Figure 3.

From these eight t_{rec} measurements we obtained a weighted median $t_{\text{rec}} = 8196 \pm 177$ s (95% confidence level; blue lines in the left panel of Figure 3). A simple weighted constant fit gave post-fit residuals with reduced chi-squared $\chi_{\text{red}}^2 = 8.1$ (7 degrees of freedom, dof), indicating unmodeled variability in the burst rate. A decreasing trend in t_{rec} can be seen, and fitting the temporal evolution with a linear model yielded $t_{\text{rec}} = -270 \pm 110$ s day $^{-1}$ (95% confidence level; orange lines in the left panel of Figure 3), and a corresponding $\chi_{\text{red}}^2 = 3.2$ (6 dof). To account for the extra scatter beyond the quoted statistical uncertainties, we modeled the t_{rec} values as Gaussian-distributed around either a constant or a linear trend, with an additional intrinsic scatter term σ_{int} added in quadrature to the individual statistical errors, and fitted both models by maximum likelihood estimation. Under the constant model we obtained $\mu = 8212$ s and $\sigma_{\text{int}} \simeq 130$ s, while the linear model gave $\mu = 8338$ s, $t_{\text{rec}} = -234$ s day $^{-1}$ and $\sigma_{\text{int}} \simeq 70$ s. A likelihood-ratio test between these two models, calibrated with a parametric bootstrap using 2000 simulations, yielded a p -value of $\simeq 0.02$ for a non-zero slope, and a bootstrap 95% confidence interval for the slope of $[-3.6, -1.1] \times 10^2$ s day $^{-1}$, indicating modest but statistically significant evidence for a decrease of t_{rec} during the outburst.

In the type-I X-ray bursters, a decreasing trend in t_{rec} typically points to an increase in the accretion rate and hence in the observed persistent flux (see Section 4.5 for a more detailed discussion). Motivated by this, we also analyzed the *NuSTAR* persistent-emission light curves in the 3–10 keV and 10–79 keV bands. As with the t_{rec} analysis, we fitted both a constant and a linear model using maximum likelihood with an

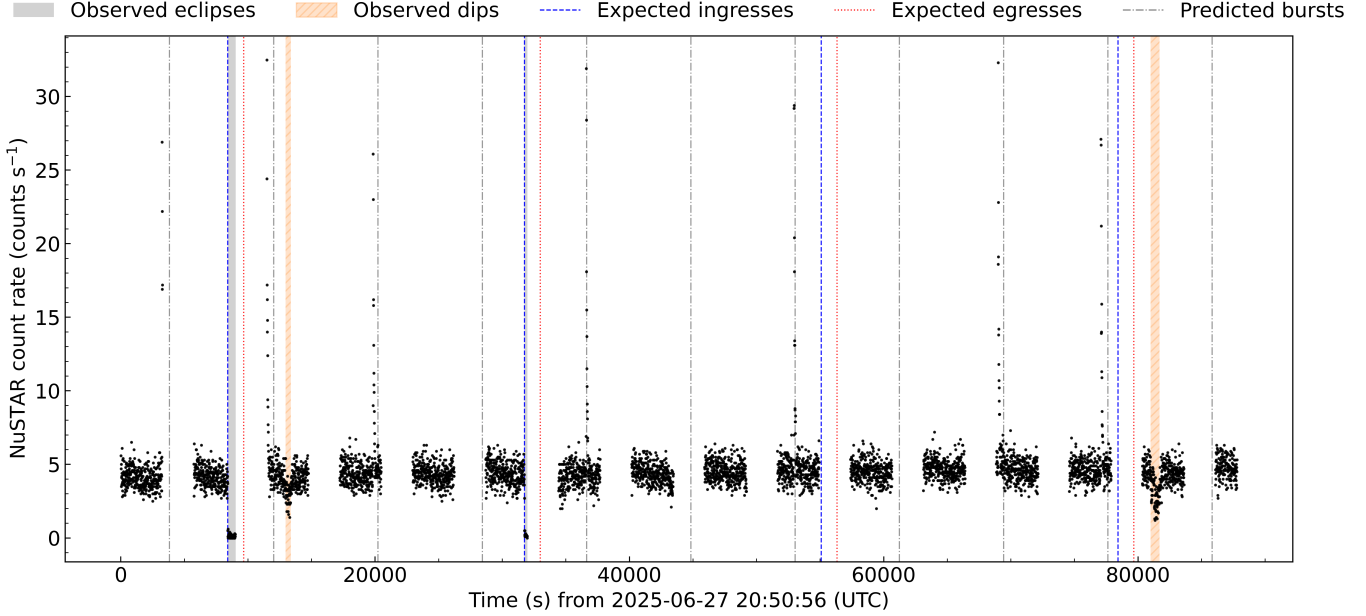


Figure 2. X-ray light curve of EP J1711–3332 obtained in the *NuSTAR* observation. The dot-dashed gray lines mark the expected epochs of bursts, using the epoch of the fourth burst as a reference and assuming a constant t_{rec} of 8200 s. The expected ingress (dashed blue lines) and egress (dotted red lines) epochs of eclipses are calculated from ObsID 11900304129. The shaded gray areas are the observed eclipse periods. The orange hatched bands are the observed dips. A total of seven bursts, two eclipses and two dips were detected during this observation.

intrinsic-scatter term σ_{int} . In both energy bands, a linear increase is strongly preferred (right panel of Figure 3). For the 10–79 keV band, we obtained, under the linear model, a slope of $0.097 \text{ cts s}^{-1} \text{ day}^{-1}$ with $\sigma_{\text{int}} \simeq 0.018 \text{ cts s}^{-1}$. A likelihood-ratio test calibrated by 2000 bootstrap simulations gave $p < 10^{-3}$, indicating a highly significant increasing trend. Similarly, in the 3–10 keV band we obtained a slope of $0.40 \text{ cts s}^{-1} \text{ day}^{-1}$ and $\sigma_{\text{int}} \simeq 0.071 \text{ cts s}^{-1}$, with a likelihood-ratio $p < 10^{-4}$. In both cases, the intrinsic scatter term makes the residuals compatible with Gaussian noise, and the bootstrap-calibrated likelihood-ratio test confirms the strong preference for a linear increase of the persistent flux during the observation. Furthermore, we attempted to fit the correlation between t_{rec} and the observed count rate with a power-law model, but we were not able to obtain acceptable fits due to the scatter in t_{rec} .

3.2. Timing analysis of eclipses and dips in X-rays

Apart from the type-I X-ray bursts, the light curves of EP J1711–3332 obtained by both EP/FXT and *NuSTAR* clearly demonstrated two more types of prominent variabilities, eclipses and dips.

We first investigated the periodicity of the eclipses by applying the Bayesian block algorithm (J. D. Scargle et al. 2013) to photon arrival times in each observation. This method identifies statistically significant changes in the source count rate and is well-suited to detect-

ing the sharp transitions expected during eclipse events. Eclipses were identified as intervals during which the count rate dropped to the background level. The start of each eclipse (ingress) was defined as the beginning of the block immediately following a sharp decline in count rate, while the end (egress) was defined as the termination of the block preceding a sharp recovery to the out-of-eclipse level. The statistical uncertainty on each ingress and egress time was conservatively estimated as half the interval between the last photon before and the first photon after the identified block edge.

Only one complete eclipse was observed in our dataset (EP/FXT, ObsID 11900304129; see Figure 4), while the remaining events were either ingress-only or egress-only detections. This was primarily due to the limited duration of the good time intervals, which often started or ended during the eclipse itself. In total, we identified seven ingress and two egress times across six distinct eclipses.

To assign integer cycle numbers to each event, we used a provisional orbital period estimated from the separation between consecutive ingress times observed with *NuSTAR* (Figure 2). We also adopted a provisional eclipse duration of $D_{\text{obs}} \approx 1260$ s, measured from the complete eclipse, to provide a consistent phase reference for all eclipses, including the partial ones.

The mid-eclipse time of the n^{th} orbital cycle (M_n) is defined as $M_n = T_0 + nP_{\text{orb}}$, where T_0 is the refer-

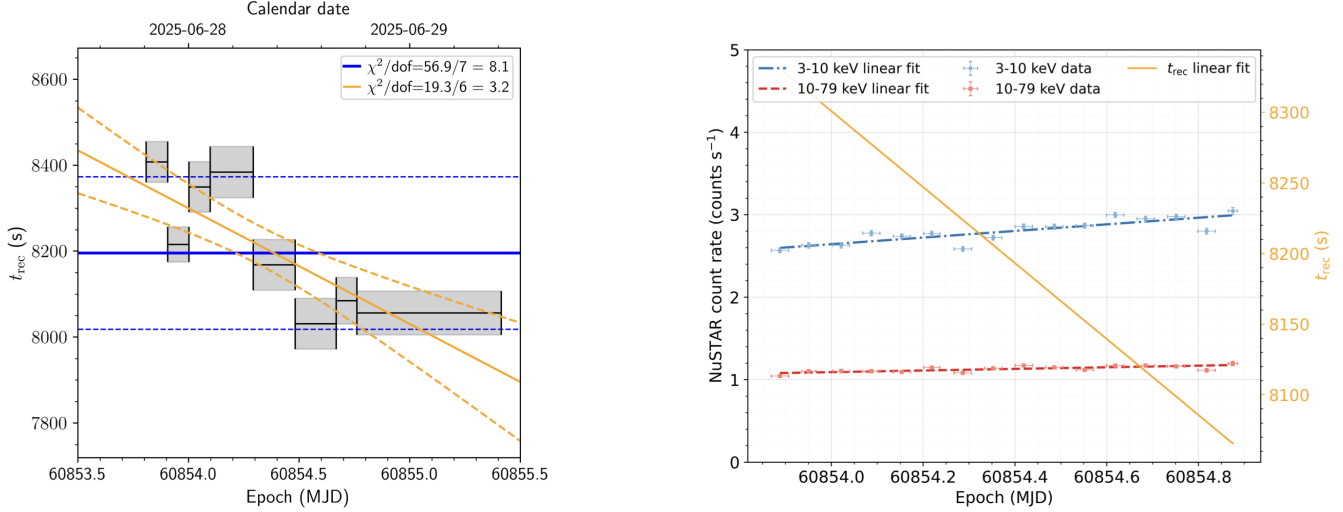


Figure 3. Left: measured recurrence times t_{rec} (black) for the eight consecutive pairs of bursts with unambiguous cycle counts. The grey shaded regions denote the validity range of each measurement, extending from the start of one burst to the start of the subsequent burst. The first burst in the first t_{rec} measurement corresponds to burst No. 3 in Table A2, while the final burst in the last measurement corresponds to burst No. 11. The blue solid and dashed lines show the weighted median recurrence time, $t_{\text{rec}} = 8196 \pm 177$ s, which does not adequately describe the data ($\chi^2_{\text{red}} = 8.1$). The orange solid and dashed lines represent a linear fit to the t_{rec} measurements, indicating a decreasing trend of $\dot{t}_{\text{rec}} = -270 \pm 110$ s day $^{-1}$, with an improved fit quality ($\chi^2_{\text{red}} = 3.2$). Right: *NuSTAR* light curves in 3–10 keV (blue) and 10–79 keV (red) bands and their respective linear fits. The *NuSTAR* data were binned over individual observational segments to improve the signal-to-noise ratio. The linear fit for t_{rec} (orange) from the left panel is also plotted on top of the light curves. The count rates in both bands show an increasing trend, with best-fit slopes of $0.40 \text{ cts s}^{-1} \text{ day}^{-1}$ (3–10 keV) and $0.097 \text{ cts s}^{-1} \text{ day}^{-1}$ (10–79 keV). Quoted errors are at 95% confidence level.

ence mid-eclipse epoch for cycle zero, and P_{orb} is the orbital period. The ingress and egress times are modeled as $T_{\text{ingress}}^{(n)} = M_n - \frac{D_n}{2}$, $T_{\text{egress}}^{(n)} = M_n + \frac{D_n}{2}$, where D_n is the eclipse duration for cycle n . Rather than assuming a fixed eclipse duration, we model each D_n as a random draw from a parent Gaussian distribution with mean $D_{*,X}$, representing the typical eclipse duration, and standard deviation σ_D , which captures intrinsic variability from cycle to cycle. The joint posterior over the model parameters was sampled using Markov Chain Monte Carlo (MCMC; W. K. Hastings 1970) techniques. We measured $P_{\text{orb}} = 6.48301 \pm 0.00003$ hr, $T_0 = 60852.62254(6)$ MJD, $D_{*,X} = 1245.5^{+6.9}_{-6.5}$ s and $\sigma_D = 14.0$ s (95% upper limit: 68.6 s). Uncertainties represent the 16th and 84th percentiles of the marginal posterior distributions.

Apart from the eclipses, we also identified a total of six dip events with the Bayesian block algorithm: two in the *NuSTAR* observation (Figure 2) and four in the EP/FXT dataset (Figure 5). Similar to eclipses, dips also involve significant rises and drops in the count rate, but they were distinguished from eclipses because of their irregular recurrence and variable duration. Moreover, during the dip events, the count rate never dropped to the background level as was the case for eclipses, and the light curve demonstrated irregular short-term variations that never occurred in eclipses. These differences

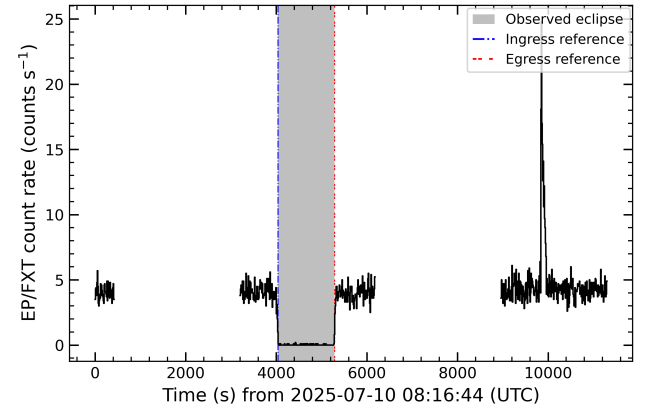


Figure 4. X-ray light curve of EP J1711–3332 from ObsID 11900304129. This is the only EP/FXT observation where an entire eclipse event was captured. We use the ingress and egress epochs observed in this eclipse event as reference points to calculate the expected ingress and egress epochs in other observations. See Figure A1 for all the FXT light curves.

point to fundamentally different physical mechanisms behind these two types of events. We note that, in order to mitigate the impact of random short-term sta-

tistical fluctuations, we conservatively retained only the detected dip candidates which lasted for over 100 s.

3.3. Searches for coherent pulsations and burst oscillations

We used the pulsar timing software package **PRESTO** (S. M. Ransom 2011) to perform Fourier-domain accelerated searches for coherent signals in the data collected during the persistent emission periods by both EP/FXT and *NuSTAR*. Data were divided into chunks with a length of 2.3 ks, corresponding to roughly one tenth of the orbital period estimated from the periodic recurrence of the eclipses. We chose this segment duration to maximize sensitivity (proportional to $\sqrt{T_{\text{obs}}}$, where T_{obs} is the duration of the observation) while avoiding the loss of power caused by non-linear acceleration Doppler smearing, known to be significant for T_{obs} higher than $\sim P_{\text{orb}}/10$ (S. M. Ransom 2001; S. M. Ransom et al. 2002; B. C. Andersen & S. M. Ransom 2018). No statistically significant signals were found. The best constraint on the pulsed-fraction upper limit was obtained with ObsID 06800000720, which is 11% (99% confidence level, in 0.5–10 keV band). We also performed the same analysis within 0.5–2 keV and 2–10 keV bands in order to separate the emissions from disk and corona, and the derived pulsed-fraction upper limits are 13% (ObsID 06800000724) and 22% (ObsID 06800000720), respectively.

We also searched for burst oscillations in each type-I X-ray burst using sliding Fourier windows of 1, 2, and 4 s duration. For each burst, the search covered the interval from 10 s before the burst onset to the end of the burst, corresponding to a total duration of approximately 130 s. Power spectra were computed in the frequency range of 50–2000 Hz using Leahy normalization. Adjacent time windows were stepped by half of the window length. The total number of independent trials per burst was therefore $\sim 1.4 \times 10^6$, accounting for the number of time windows, frequency bins, and window lengths. No statistically significant oscillation signal was detected after correcting for the number of trials. We derived upper limits on the fractional rms amplitude by converting the detection-threshold power to rms amplitude using $r_{\text{rms}} = \sqrt{P_{\text{th}}/2N}$, where N is the total number of photons in each time window. For a global 3σ confidence level, this corresponds to a Leahy-normalized power threshold of $P_{\text{th}} \approx 40$.

This analysis was performed for the eight bursts observed by EP/FXT in TM, and the resulting 3σ upper limits on the oscillation amplitude depend on the burst brightness and integration time. The most constraining limits we obtained are approximately 65–84% rms for 1-s windows, 49–68% rms for 2-s windows, and 36–50% rms for 4-s windows, with the tightest constraints obtained from the brightest bursts and the longest integration times. For *NuSTAR* bursts, with the same analysis, the limits we derived are 49–58% rms for 1-s windows,

35–41% rms for 2-s windows, and 27–31% rms for 4-s windows.

3.4. X-ray spectral analysis

3.4.1. Persistent emission

In this section, we report on the spectral analysis of the persistent emission from EP J1711–3332 excluding both bursts and eclipses. All EP/FXT and *NuSTAR* spectra were grouped using the optimal binning following J. S. Kaastra & J. A. M. Bleeker (2016), while maintaining at least 25 counts per bin to allow the use of χ^2 statistics. Spectral fits were performed with **Xspec** v12.12.1. In all cases, we applied the **TBabs** model to account for interstellar absorption, adopting photoelectric cross-sections and elemental abundances from D. A. Verner et al. (1996) and J. Wilms et al. (2000), respectively. When combining data from multiple instruments, a **constant** component was added to account for cross-calibration uncertainties, and we verified that differences in the constant values between instruments remained within 20%.

With the aim to perform a broadband spectral analysis, we paired our *NuSTAR* spectrum with all the EP observations performed within the *NuSTAR* observing window, i.e., ObsIDs 0680000699, 0680000706 and 0680000707 (see Table A1 for more details). An initial exploratory fit with a simple **TBabs** × **powerlaw** model (Model 0) was found unacceptable, as significant unmodeled residuals were present below 2 keV and around 7 keV (see Figure 6). The residuals indicate the presence of both a soft thermal component and reflection features. We therefore adopted a more physically motivated model. The **powerlaw** component was replaced with a **bbodyrad** convolved with **thcomp** (A. A. Zdziarski et al. 2020), to jointly model the Comptonization and the seed photon spectra. To represent the soft thermal emission, we added a **diskbb** component. Reflection was accounted for using the self-consistent **relxillcp** model (J. García et al. 2014), which describes reflection of a Comptonized continuum off the accretion disk. To capture the low-energy roll-over in the seed photon spectrum — unaccounted for in **relxillcp**, which assumes a fixed and unrealistically low seed temperature of 0.05 keV — we included an **expabs** multiplicative component, characterized by the cut-off energy $E_{\text{cut-off,low}}$ parameter. Despite the inclusion of reflection, residual absorption features remained near ~ 7 keV, prompting us to add a **gaussian** absorption line. Our final model reads therefore:

$$\text{Model 1: } \text{TBabs} \times (\text{thComp} \times \text{bbodyrad} + \text{diskbb} + \text{expabs} \times \text{relxillcp} + \text{gaussian})$$

An overview of all the parameters included in the model is reported in Table 1. For physical consistency, we tied $E_{\text{cut-off,low}}$ to $3 \times kT_{\text{bb}}$, the photon indices Γ and electron temperatures kT_{e} of **thcomp** and **relxillcp**

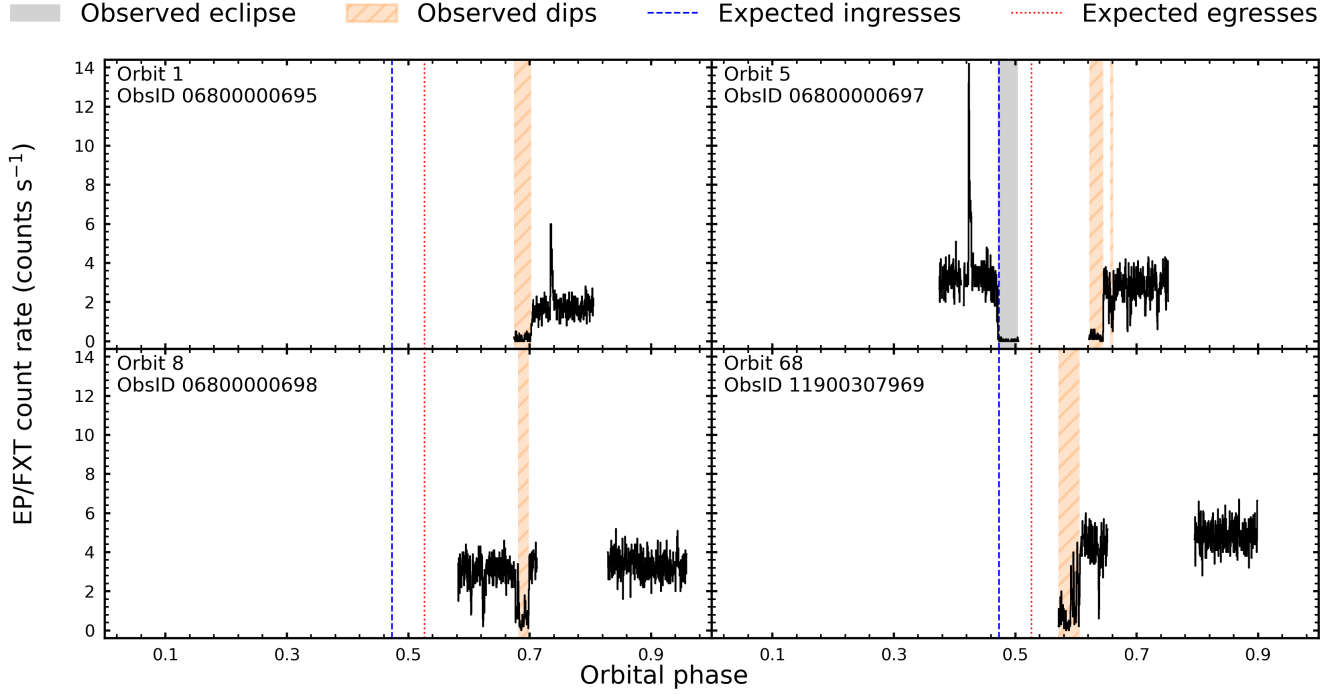


Figure 5. Phase-resolved light curves of four EP/FXT observations with dips (orange hatched bands). Each panel shows the data obtained over one orbit of the binary system. The orbit observed by the first FXT observation is defined as Orbit 1. The expected ingress (dashed blue lines) and egress (dotted red lines) epochs are calculated from ObsID 11900304129. The shaded gray area is the observed eclipse period. See Figure A1 for all the FXT light curves.

and fixed the reflection fraction parameter f_{ref} to -1 to only consider the reflection spectral component. Some parameters were not well constrained by the fit, so that we froze them to typically adopted values for LMXBs (e.g. A. Marino et al. 2022; R. M. Ludlam 2024; C. Malacaria et al. 2025; F. La Monaca et al. 2025), i.e., the emissivity index ϵ to 3, the Fe abundance A_{Fe} to 1, the density parameter $\log N$ to 20. For the binary inclination i , which was also not well constrained by the fit due to degeneracies, we fixed the value to 74° (see Section 4.1 for the discussion on the binary inclination i).

In order to investigate the long-term evolution of the persistent emission, we performed similar spectral analysis for the rest of the FXT observations as well. Due to a lack of high-energy coverage above 10 keV and the absence of clear residuals due to reflection when only FXT data are available, we removed `relxillCp` from the spectral model, thus adopting a simplified version that reads: $\text{TBabs} \times (\text{thComp} \times \text{bbodyrad} + \text{diskbb})$. To better constrain the parameters, during spectral fitting, we fixed the values of the hydrogen column density (N_{H}), electron temperature of the corona (kT_{e}) and blackbody temperature (kT_{bb}) to the values derived from the joint fitting with *NuSTAR* (see Table 1), and the value of covering fraction (f_{cov}) to 1. Data collected by both FXT-A and FXT-B were used for spectral analysis, except that for TM we ignored the data below 1 keV and

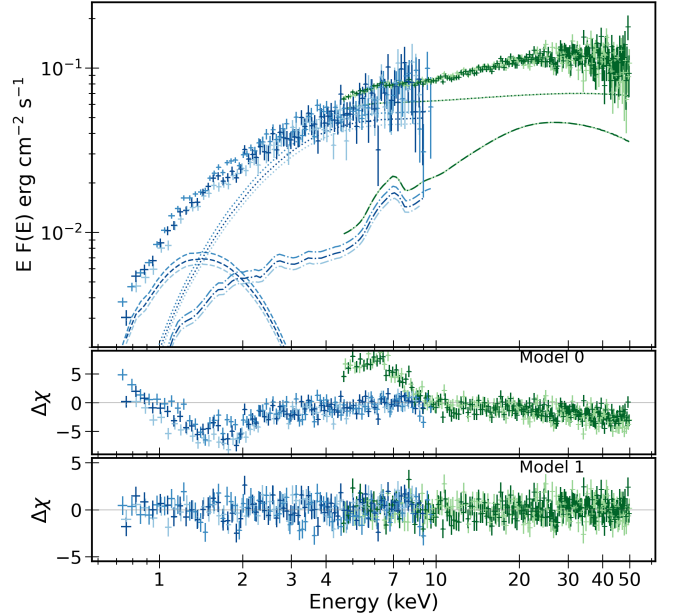


Figure 6. Broadband EP/FXT (blue) and *NuSTAR* (green) spectra with the best-fit Model 1 (top panel), and residuals from Model 0 (middle panel) and Model 1 (bottom panel). Different line styles were adopted to distinguish between the different components: dot for `diskbb`, dash for `thcomp` \times `bbodyrad` and dash-dot for `relxillCp`.

Broadband spectral analysis for the persistent emission				
Component	Parameter	Unit	Description	Value
constant	c_{cal}		Intercalibration constant	(1.0)
TBabs	N_{H}	10^{22} cm^{-2}	Equivalent hydrogen column density	$0.48_{-0.07}^{+0.08}$
expabs	$E_{\text{cut-off,low}}$	keV	Low energy cut-off	$= 3 \times kT_{\text{bb}}$
relxillCp	i	$^{\circ}$	Binary inclination	(74.0)
	a^*		Spin parameter	(0)
	R_{in}	R_g	Inner disk radius	38_{-9}^{+14}
	R_{out}	R_g	Outer disk radius	(1000)
	ϵ		Disk emissivity	(3.0)
	z		Redshift to the source	(0)
	Γ_{relxill}		Power-law index of the incident spectrum	$= \Gamma$
	$\log \xi$		Disk ionization	$2.13_{-0.09}^{+0.10}$
	$\log N$	cm^{-3}	Disk density	(20.0)
diskbb	A_{Fe}		Fe abundance of reflecting material	(1.0)
	$kT_{\text{e,refl}}$	keV	Electron temperature of the corona	$= kT_e$
	f_{refl}		Reflection fraction	(-1.0)
	K_{refl}		Reflection normalization	$0.0021_{-0.0008}^{+0.0004}$
	kT_{disk}	keV	Inner disk temperature	$0.30_{-0.05}^{+0.25}$
	K_{disk}		Disk normalization	400_{-280}^{+890}
gaussian	E_{line}	keV	Line centroid energy	(6.97)
	σ_{line}	keV	Line width	(0.2)
	K_{line}		Line normalization	$-(6.0 \pm 2.0) \times 10^{-5}$
thComp	Γ		Power-law index of the Comptonization spectrum	$1.90_{-0.03}^{+0.04}$
	kT_e	keV	Electron temperature of the corona	22_{-3}^{+20}
	f_{cov}		Covering fraction	(1.0)
bbodyrad	kT_{bb}	keV	Blackbody temperature	$0.80_{-0.08}^{+0.30}$
	K_{bb}		Blackbody normalization	28_{-17}^{+11}
cflux	$F_{1-10 \text{ keV}}$	$(\times 10^{-10}) \text{ erg cm}^{-2} \text{ s}^{-1}$	X-ray unabsorbed flux	2.070 ± 0.008
	χ^2/ν		reduced χ^2 for ν degrees of freedom	544/526

Table 1. Results of the broadband spectral analysis for the persistent emission. Quoted errors reflect 90% confidence level. The parameters that were held constant during the fits are reported between round parentheses. R_g represents the gravitational radius. The reported flux values correspond to the 1–10 keV energy range.

the data above 9 keV due to known calibration issues (private communication). The unfolded EP/FXT spectra and the spectral fitting residuals are shown in Figure A2. The evolution of the key spectral parameters is shown in Figure 7 and a detailed discussion is given in Section 4.4.

3.4.2. Type-I X-ray burst emission

We first performed time-averaged spectral analysis for each burst. For the seven bursts in the *NuSTAR* dataset (Table A2), the **Xspec** model adopted in the analysis is **TBabs** × (**nthComp** + **bbodyrad**), where **nthComp** is used to account for the persistent emission during the burst and **bbodyrad** models the burst spectrum. During the spectral fitting, the values of N_{H} , Γ , kT_e , kT_{bb} (note that

kT_{bb} here is a parameter of **nthComp**, representing the temperature of the seed photons for Comptonization) were fixed to those derived from the broadband spectral analysis of the persistent emission (Table 1). For each burst, we used the pre-burst persistent spectrum as background. A similar analysis was also performed for bursts in the EP/FXT dataset (Table A2), adopting a simplified model of **TBabs** × **bbodyrad** due to the limited bandpass of FXT. The fitting results, including the averaged unabsorbed bolometric (0.01–100 keV) flux ($F_{\text{bst,bol}}$), burst temperature ($kT_{\text{bst,bb}}$) and normalization ($K_{\text{bst,bb}}$), are presented in Figure A3 and Figure A4, respectively for *NuSTAR* bursts and FXT bursts. In all 16 bursts, the averaged burst temperature has a simi-

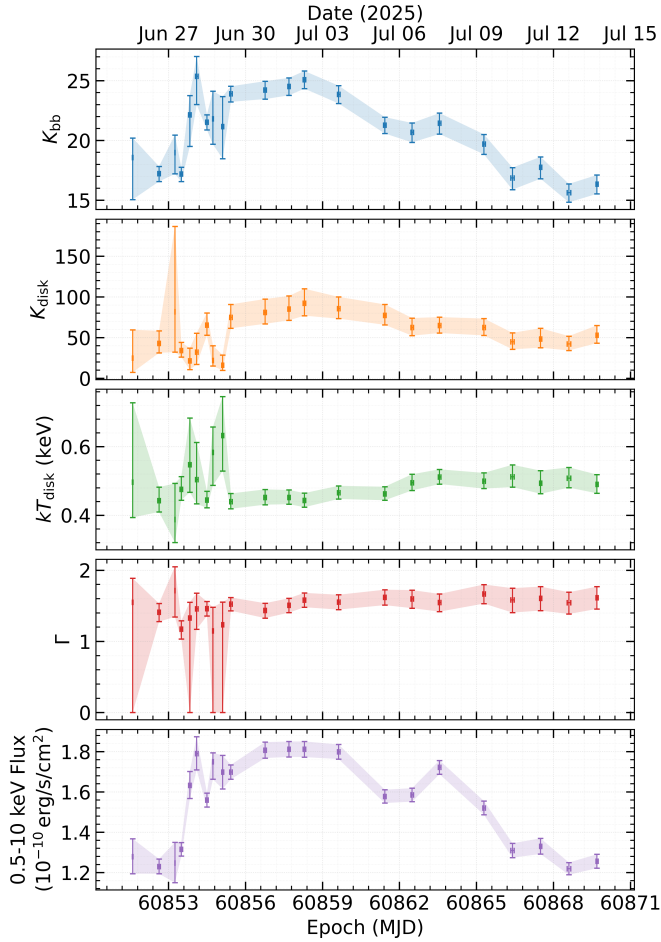


Figure 7. Evolution of key spectral parameters from the 22 FXT observations presented in this work. The model adopted for spectral analysis is $\text{TBabs} \times (\text{thComp} \times \text{bbodyrad} + \text{diskbb})$. The reported flux is the observed flux. Shaded areas denote uncertainties at 90% confidence level.

lar value of $kT_{\text{bst,bb}} \approx 1.4 - 1.8 \text{ keV}$, although $F_{\text{bst,bol}}$ varies from $\sim 1.7 \times 10^{-10} \text{ erg cm}^{-2} \text{ s}^{-1}$ (burst No. 5) to $\sim 7.0 \times 10^{-10} \text{ erg cm}^{-2} \text{ s}^{-1}$ (burst No. 15).

We also performed time-resolved spectral analysis for all the bursts. For each burst, we divided the whole time span into several segments and performed spectral fitting for each segment with the same models adopted for the time-averaged analysis. For *NuSTAR* bursts we further tied the normalization of `nthComp`, K_{Comp} , across the different segments in order to better constrain the variations of the `bbodyrad` model parameters used to describe the thermal emission during the bursts, given the relatively low count statistics in each segment. We were able to derive acceptable fits (with $\chi^2_{\text{red}} < 1.5$) and constrain the spectral parameters for most of the time segments. The evolution of $F_{\text{bst,bol}}$, $kT_{\text{bst,bb}}$ and $K_{\text{bst,bb}}$ for each burst is presented in Figure A5 (*NuSTAR*) and Figure A6 (EP/FXT). We found no evidence for photospheric radius expansion (see e.g. W. H. G.

Lewin et al. 1993) in either of the datasets, implying that the burst luminosities are sub-Eddington. The peak burst temperature can reach $\sim 2 \text{ keV}$ (e.g. burst No. 7) and the peak bolometric flux during the bursts is $\sim 2.6 \times 10^{-9} \text{ erg cm}^{-2} \text{ s}^{-1}$ (burst No. 16).

Burst No. 8 was simultaneously detected by both *NuSTAR* and EP/FXT, providing an excellent opportunity to investigate its spectral evolution over a broad energy range. We performed time-resolved spectral analysis from the onset to the end of the burst using time bins of 5 s, 10 s, 20 s, and 50 s, combining data from both instruments. We adopted two different methods to analyze the burst spectra. The first is the standard approach, commonly referred to as the “classical” method, which assumes that the persistent emission remains unchanged before and during the burst. This is also the method applied to the other 15 bursts. In this method, the 100 s pre-burst spectrum was used as the background in the spectral fitting and the burst emission was modeled with $\text{TBabs} \times \text{bbodyrad}$ in *XSPEC*. The second method is the so-called f_a method (H. Worpel et al. 2013), which allows the persistent emission to vary in intensity during the burst while assuming that its spectral shape remains unchanged. We adopted the $\text{TBabs} \times (\text{nthComp} + \text{bbodyrad})$ model and allowed only K_{Comp} to vary, thereby accounting for changes in the persistent emission during the burst.

The spectral analysis results are presented in Figure A7. At the onset of burst No. 8, the bolometric flux rises rapidly to a peak of $\sim (2 - 3) \times 10^{-9} \text{ erg cm}^{-2} \text{ s}^{-1}$, accompanied by a high blackbody temperature of $kT_{\text{bst,bb}} \approx 2.0 - 2.2 \text{ keV}$. During the subsequent decay phase, the flux decreases monotonically, while $kT_{\text{bst,bb}}$ shows a gradual cooling trend toward $\sim 1.5 - 1.7 \text{ keV}$. In contrast, $K_{\text{bst,bb}}$ initially increases around the burst peak and then declines, consistent with the cooling tail behavior commonly observed in thermonuclear bursts. The results obtained with the classical and f_a methods are broadly consistent in terms of the overall flux and temperature evolution. However, the f_a method indicates a significant enhancement of the persistent emission during the early phase of the burst, as reflected by an increase in K_{Comp} that peaks near the burst maximum and subsequently decreases toward the pre-burst level. This suggests that the burst temporarily amplifies the persistent emission component, while the intrinsic burst emission follows a standard cooling evolution trend.

3.4.3. Ratio of accretion energy to thermonuclear energy

The above spectral-timing analysis allowed us to evaluate another key parameter, the ratio between the accretion energy released in the interval between two consecutive bursts and the thermonuclear energy released during the second burst (α). Among the 16 bursts detected, there are only three pairs of bursts that were consecutive, i.e., no more bursts likely occurred in be-

tween. Specifically, the three pairs are bursts No. 4–5, No. 5–6 and No. 9–10, which allowed us to estimate α for bursts No. 5, 6 and 10. For each of the three pairs, we performed spectral fitting both for the burst and for the persistent emission between the bursts using the same methods described in Section 3.4.1 and Section 3.4.2, and we estimated the bolometric fluxes by extrapolating the best-fit models to the 0.01–100 keV band. For simplicity, we assumed that the burst and persistent emission have the same anisotropy factors. α was then derived as the ratio between the bolometric fluence of the persistent emission and that of the burst. We estimated $\alpha \approx 130$ for bursts No. 5 and 6, and $\alpha \approx 120$ for burst No. 10. The implication of these values is discussed in Section 4.5.

3.5. The optical counterpart

We constructed light curves for all of the stars within the various X-ray, radio and optical error circles reported in Section 1. Only one target (see Figure 8 for the optical image) showed any significant variability. Moreover, this variability is in the form of an optical eclipse that coincides with the time of the X-ray eclipse — further discussed in Section 3.5.1 — giving us great confidence that we have indeed identified the optical counterpart.

3.5.1. The optical eclipse

Using the simultaneous ULTRACAM and EP observations, we studied the eclipse duration over different energy bands. Figure 9 shows that the optical flux exhibits a smooth transition during the eclipses, in stark contrast to the sharp behavior observed in the X-rays. In order to model specifically these differences, we fit each optical light curve with a piecewise-linear trapezoidal model (after removing the flare, see Section 3.5.2) that includes seven free parameters: the out-of-eclipse flux levels (allowed to differ before and after the eclipse), the in-eclipse flux, the ingress start time, and the durations of the three segments. The profile of the trapezoidal model is flat outside the eclipse, linear during ingress and egress, and constant during totality. Fits were performed over a time interval fully covering the eclipse and displaying stable out-of-eclipse emission, by means of a non-linear least-squares algorithm. Parameter uncertainties were derived from 300 bootstrap realizations per band, where synthetic light curves were generated by perturbing the best-fit model with Gaussian noise and refitting them.

The analysis was repeated using several bin sizes between 50 and 100 s, given that the parameter values may depend to some extent on the temporal binning of the light curves. Across all tested binnings, the total eclipse duration ranges from $D_{\star,g} \approx 1370$ –1610 s in the g_S band to $D_{\star,i} \approx 1570$ –2015 s in the i_S band. Thus, the i_S -band eclipse is consistently longer than in the g_S -band by ≈ 200 –400 s, with a statistical significance of $\gtrsim 3\sigma$ across all tests. We also measured the eclipse depth, defined

as the difference between the average out-of-eclipse flux and the flux during totality, expressed as a fraction of the out-of-eclipse level. Across all sampled binnings, the eclipse removes $\approx 50\%$ of the g_S -band flux and $\approx 35\%$ of the i_S -band flux.

Combined with the X-ray eclipse results (see Section 3.2), our measurements show that the eclipse is shorter and removes a larger fraction of the emission at shorter wavelengths, revealing a clear wavelength dependence in the occulted component.

3.5.2. The optical flare

The ULTRACAM light curves reveal an optical flare that occurred entirely during the eclipse and lasted a few minutes (Figure 9). It is likely a real feature and not an artifact as it was visible in both bands, and it does not correlate with variations in the seeing, transparency or object positions on the CCD. The flare reached a peak intensity exceeding the out-of-eclipse level of the persistent optical emission. The color evolution, shown in the bottom panel of Figure 9, indicates that the emission becomes slightly bluer at the flare peak.

4. DISCUSSION

EP J1711–3332 is a new NS-LMXB discovered in outburst by *Einstein Probe* on 2025 June 23. It exhibited rare behaviors including clocked bursts, eclipses and dip events. In this section we discuss in detail these phenomena and their implications, as well as the spectral properties of the persistent emission.

4.1. Properties of the binary system

With the knowledge of the orbital period determined from the eclipses, i.e. $P_{\text{orb}} \approx 6.48$ hr (see Section 3.2), we can give a rough estimate of the mass and radius of the companion star. [P. P. Eggleton \(1983\)](#) derived the effective radius of the Roche lobe (R_L) as

$$\frac{R_L}{a} = \frac{0.49q^{2/3}}{0.6q^{2/3} + \ln(1 + q^{1/3})}, \quad (1)$$

where $q = M_2/M_1$, with M_1 and M_2 being the masses of the NS and the companion, respectively. a is the orbital separation of the system given by

$$\frac{a}{R_\odot} \approx 0.51 \left(\frac{M_1 + M_2}{M_\odot} \right)^{1/3} P_{\text{orb}}^{2/3}. \quad (2)$$

We further introduced a filling factor defined as $\beta \equiv \frac{R_2}{R_L}$, where R_2 is the companion radius. This yielded a mass-radius relation for the companion star,

$$\frac{R_2}{R_\odot} = \frac{0.245\beta q^{2/3}((M_1 + M_2)/M_\odot)^{1/3} P_{\text{orb}}^{2/3}}{0.6q^{2/3} + \ln(1 + q^{1/3})}. \quad (3)$$

To solve for both R_2 and M_2 , another mass-radius relation is required, for which we tested three relations available in literature: the empirical mass-radius relation for

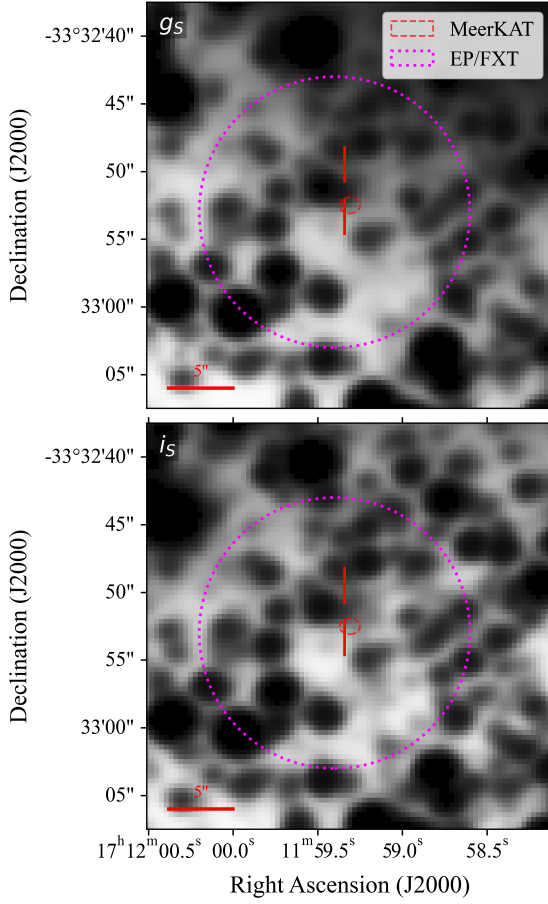


Figure 8. A deep stack of the 2.2 hours of optical data obtained with ULTRACAM in the g_s (top) and i_s (bottom) bands. The 785 images were individually shifted to account for image motion prior to adding together. The images shown are $30''$ on a side. North is up and East to the left. The optical counterpart is indicated with the red tick marks. The positional error regions of the X-ray source (EP/FXT) and the radio counterpart (*MeerKAT*) are overlaid.

single low-mass ($M_2 < 1.66M_\odot$) main-sequence stars (O. Demircan & G. Kahraman 1991), the mass-radius relation derived with a sample of companion stars in cataclysmic variables (CVs; but LMXBs appear to follow a similar trend; D. A. Smith & V. S. Dhillon 1998), and a more recent relation which also applies to Roche-lobe filling CV donors (M. McAllister et al. 2019). Assuming $\beta \approx 1$ and a typical NS mass of $M_1 = 1.4M_\odot$, the three relations give broadly consistent values of $M_2 \approx 0.6 - 0.8M_\odot$ and $R_2 \approx 0.7 - 0.8R_\odot$. These are consistent with a K-type star.¹⁹ Moreover, D. A. Smith & V. S. Dhillon (1998) provided an empirical relation

¹⁹ Based on the relation between stellar mass and spectral type provided in A Modern Mean Dwarf Stellar Color and Effective Temperature Sequence. See also M. J. Pecaut & E. E. Mamajek (2013).

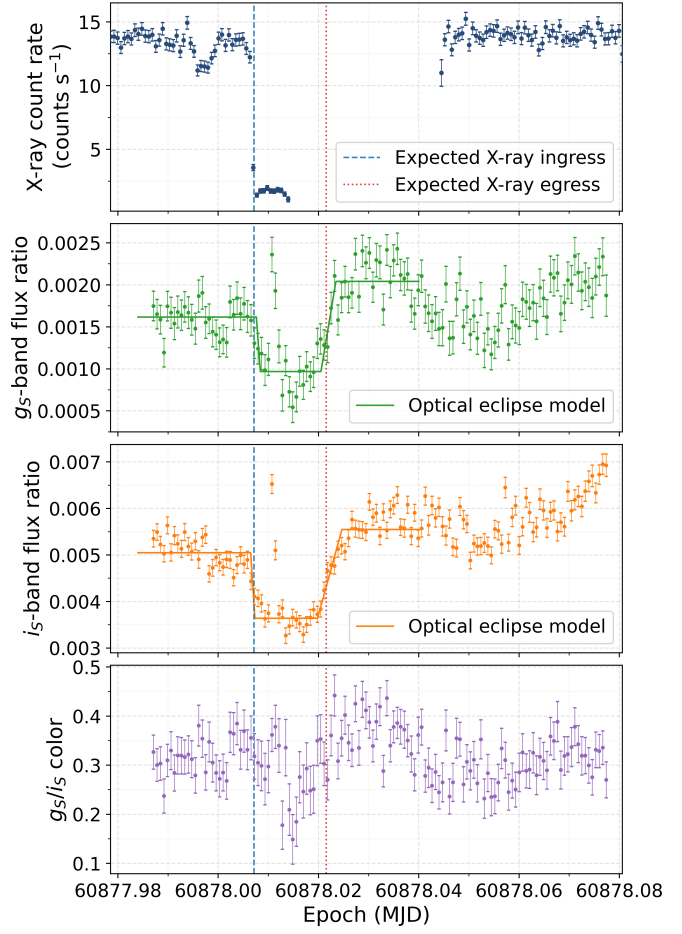


Figure 9. Top panel: X-ray light curve collected by EP/FXT. Second and third panels: ULTRACAM light curves in g_s -band and i_s -band, expressed as the flux ratio between the target and the comparison star. The details of the superimposed optical eclipse models (green and orange solid lines) can be found in the text. Bottom panel: the optical color computed as the ratio between g_s -band and i_s -band fluxes. In all panels, the expected X-ray ingress (dashed blue lines) and egress (dotted red lines) epochs are calculated from ObsID 11900304129. The data are rebinned at a time resolution of 60s.

between the companion spectral type and the orbital period for CVs and LMXBs, which, with $P_{\text{orb}} \approx 6.48$ hr, predicts a spectral type of K7 with a range of K4 to M0, confirming our previous estimate.

The inclination of an eclipsing system can be expressed by

$$\sin i \approx \frac{\sqrt{1 - (R_2/a)^2}}{\cos \theta_{\text{ec},X}}, \quad (4)$$

where $\theta_{\text{ec},X}$ is the eclipse half-angle, which can be estimated as $\theta_{\text{ec},X} = \pi D_{*,X}/P_{\text{orb}}$ (P. C. Joss & S. A. Rappaport 1984). From the above, we estimate a high binary inclination of $i \approx 73 - 75^\circ$.

The longer and shallower eclipses seen in the optical bands indicate that a substantial fraction of the optical emission originates in an extended region surrounding the NS. The characteristic radius of the eclipsed emitting region at wavelength λ is given by

$$R_\lambda = a \sqrt{1 - \sin^2 i \cos^2 \theta_{\text{ec},\lambda}} - R_2. \quad (5)$$

We obtain $R_{g_S} \simeq (1.39\text{--}4.87) \times 10^9 \text{ cm}$ and $R_{i_S} \simeq (4.17\text{--}10.44) \times 10^9 \text{ cm}$, indicating a larger characteristic size for the redder optical emission. The eclipse depths are likewise consistent with a progressively larger extended/uneclipsed contribution at longer wavelengths.

The optical flare detected during eclipse (see Section 3.5.2) provides additional clues about the companion. Its occurrence at a phase when the NS and the inner accretion flow are occulted, combined with the absence of any simultaneous increase in X-ray emission, rules out a thermonuclear X-ray burst with direct reprocessing as the origin. Instead, the flare properties resemble impulsive magnetic events in active late-type stars, in which a brief heating episode produces a hot, blue continuum followed by a more gradual cooling phase. The fact that the flare remains visible during eclipse implies that its emitting region is not obscured together with the NS and accretion flow. This points to the hemisphere of the Roche-lobe-filling companion facing the observer as the most likely site of emission. Overall, our interpretation is consistent with the expected magnetic activity of late-type dwarfs, as K-type stars are known to produce energetic flares (e.g. Z. Yang et al. 2023).

4.2. Constraints on the distance and luminosity

From the broadband spectral analysis with *NuSTAR* and FXT data (Table 1), we constrained the value of the hydrogen column density to $N_{\text{H}} = 0.48^{+0.08}_{-0.07} \times 10^{22} \text{ cm}^{-2}$. This result was then compared with the estimated column density curve along the line of sight in the direction of EP J1711–3332, which is accessible from the 3D- N_{H} -tool²⁰ (V. Doroshenko 2024; G. Edenhofer et al. 2024; J. M. Yao et al. 2017; Planck Collaboration et al. 2016), to estimate the source distance, d . We used a Monte Carlo method to account for the uncertainties in N_{H} and derived a lower limit of $d_{\text{min},X} \sim 1.6 \text{ kpc}$ for the distance. The peak bolometric flux of the type-I X-ray bursts we estimated in this work is $\sim 2.6 \times 10^{-9} \text{ erg cm}^{-2} \text{ s}^{-1}$ (Section 3.4.2). By limiting the corresponding peak luminosity under the Eddington luminosity ($L_{\text{Edd}} = 1.77 \times 10^{38} \text{ erg s}^{-1}$ for an NS mass of $1.4 M_{\odot}$), and assuming the emission is isotropic, we put a loose upper limit of $d_{\text{max},X} \sim 23.8 \text{ kpc}$ on the distance. This value is comparable with the approximate extent of the Galaxy in the direction of EP J1711–3332, which is $\sim 25 \text{ kpc}$.

²⁰ <http://astro.uni-tuebingen.de/nh3d/nhtool>

A better constraint on the distance can be derived using the optical data obtained by ULTRACAM. During the optical eclipse (Section 3.5.1), it is reasonable to assume that the optical emission is predominantly from the non-irradiated side of the companion star, and therefore the apparent magnitude of the star can be measured. Using SMSS 171158.71–333340.7, a bright star approximately $1.1'$ south of the target, as a calibrator, the observed optical fluxes were calibrated into magnitudes. We adopted the faintest magnitudes during the eclipse as the apparent magnitudes of the star, which are $m_{g_S} = 24.4 \pm 2.9$ (1σ uncertainty) in the g_S -band and $m_{i_S} = 20.8 \pm 0.2$ in the i_S -band. Then, tentatively assuming a spectral type of K4 to M0 (Section 4.1), the absolute magnitudes of the companion in the two bands were derived to be $M_{g_S} \approx 7.5\text{--}9.6$ and $M_{i_S} \approx 6.3\text{--}7.6$.²¹ Further considering the interstellar extinction in the two bands, $A_{g_S}(d)$ and $A_{i_S}(d)$,²² the distance of the system can be estimated by solving the following equation:

$$m_\lambda - M_\lambda = 5 \log_{10}(d/10\text{pc}) + A_\lambda(d). \quad (6)$$

We thus derived $d_{g_S} > 1.4 \text{ kpc}$ and $d_{i_S} \sim 2.0\text{--}6.4 \text{ kpc}$ from the g_S - and i_S -band data, respectively. The latter provides a tighter constraint, as the data have smaller uncertainties.

In summary, the best constraints on the distance of the system available so far are $d_{\text{min}} \sim 2.0 \text{ kpc}$ and $d_{\text{max}} \sim 6.4 \text{ kpc}$, with which the luminosity of the source can be estimated. Extrapolating the best-fit 1–10 keV spectral model presented in Table 1 to the 0.01–100 keV range, we estimated a bolometric correction factor of $K_{\text{bol}} \sim 3$. The bolometric flux at the epoch of the *NuSTAR* observation is therefore $F_{\text{bol}} \sim F_{0.01\text{--}100\text{keV}} \sim 6 \times 10^{-10} \text{ erg cm}^{-2} \text{ s}^{-1}$, which corresponds to a luminosity of $L_{\text{bol}} \sim 2.8 \times 10^{35} (d/2.0 \text{ kpc})^2 \text{ erg s}^{-1} = 2.9 \times 10^{36} (d/6.4 \text{ kpc})^2 \text{ erg s}^{-1}$. The Eddington ratio is thus $L_{\text{bol}}/L_{\text{Edd}} \sim 0.2\% \text{--} 1.6\%$.

4.3. The dip events

In both FXT and *NuSTAR* data we identified a total of six dip events (Section 3.2). Despite the significant differences in the duration and the short-term variations seen in the light curves, we note that all six dips were found to occur within the orbital phase range of $\sim 0.6\text{--}0.7$ (with the center of eclipses defined as phase 0.5), suggesting a possible correlation with the binary

²¹ The absolute magnitude in the V -band is provided in [A Modern Mean Dwarf Stellar Color and Effective Temperature Sequence](#) and the value can be transformed into those in SDSS photometry (see K. Jordi et al. 2006). Note that ULTRACAM uses “Super SDSS filters”, but here we tentatively ignored the difference for simplicity.

²² The extinction curve in the V -band was obtained with the 3D- N_{H} -tool, which was then transformed into $A_{g_S}(d)$ and $A_{i_S}(d)$ using `python` package `dust_extinction` (K. Gordon 2024; K. D. Gordon et al. 2023).

orbit. This could potentially support the interpretation that dip events arise from the obscuration of the central X-ray source by the bulge produced by the impact of matter transferred from the companion star at the outer disk (for a review, see T. Di Salvo et al. 2023). However, the occurrence of dips is still far from regular, e.g., the *NuSTAR* observation covered the 0.6–0.7 range of orbital phase also during two other orbits, yet no dips were detected, suggesting a more complicated physical mechanism behind such events.

We also note that the dips were observed only in the observations before 2025 June 28 and in the last observation on 2025 July 13, which coincide with the periods when the source flux was at a relatively low value of 1.3×10^{-10} erg cm $^{-2}$ s $^{-1}$ (Figure 7). The flux dependence of dip events was also seen in other sources, e.g. MAXI J1820+070 (J. J. E. Kajava et al. 2019) and MAXI J1659–152 (E. Kuulkers et al. 2013). The disappearance of dips at higher flux levels likely reflects changes in the ionization and vertical structure of the disk rim: as the accretion rate increases, stronger irradiation and radiation pressure can ionize or geometrically smooth the bulge at the stream–disk impact point, reducing its ability to obscure the central source.

4.4. Spectral properties of the persistent emission

We extensively monitored the spectral evolution of EP J1711–3332 with EP/FXT during the first 21 days of the outburst (see Figure 7). The source was initially detected with an observed persistent flux of $\sim 1.3 \times 10^{-10}$ erg cm $^{-2}$ s $^{-1}$ in 0.5–10 keV band, which rose to $\sim 1.8 \times 10^{-10}$ erg cm $^{-2}$ s $^{-1}$ on June 27. The flux remained roughly constant until July 7 then slowly declined back to the initial flux level of $\sim 1.3 \times 10^{-10}$ erg cm $^{-2}$ s $^{-1}$. Despite the variation in flux, the spectral shape did not show significant changes (see also Figure A2). In all the observations presented in this work, EP J1711–3332 exhibited a typical hard-state spectrum, with a low power-law photon index of $\Gamma \sim 1.5$. Moreover, from our broadband spectral analysis performed with both EP/FXT and *NuSTAR* data (see Figure 6 and Table 1), we obtained an inner disk radius of $R_{\text{in}} = 38_{-9}^{+14} R_{\text{g}}$ and a corona electron temperature of $kT_{\text{e}} = 22_{-3}^{+20}$ keV. These are also broadly consistent with those seen in the hard spectral state of NS-LMXBs (e.g. F. Pintore et al. 2018; A. Marino et al. 2022; R. M. Ludlam 2024; G. Illiano et al. 2024). We thus suggest the following accretion geometry: a truncated accretion disk with the inner region replaced by a hot accretion flow (corona), which Compton scatters soft photons emitted from a hot region on the NS surface. The area of this region is $\sim 4–36$ km 2 as measured from the blackbody normalization, using the distance of the system at $\sim 2.0–6.4$ kpc (Section 4.2).

4.5. Comparison of EP J1711–3332 with other clocked bursters

The defining observational characteristic of clocked bursters is the quasi-periodic recurrence of type-I X-ray bursts. Owing to long data gaps and intrinsic variability in the burst rate, we could not obtain a coherent periodic solution across the full 16-day dataset, which included 16 bursts. Reliable recurrence times were measured only for eight pairs of consecutive bursts spanning 1.6 days around the time of the *NuSTAR* observation. These bursts were separated by short or no observational gaps. For this subset, we found $t_{\text{rec}} = 8196 \pm 177$ s ($\nu_{\text{rec}} \approx 0.122$ mHz). The data showed a likely linear decrease in the recurrence rate of $i_{\text{rec}} = -270 \pm 110$ s day $^{-1}$, although notable scatter remains, indicating intrinsic variability in the accretion rate or burning conditions on the NS on the timescale of individual bursts (Figure 3). Additional continuous observations covering multiple consecutive bursts would be required to provide a more precise characterization of the source’s temporal behavior.

In the seven known clocked bursters, the recurrence time of bursts is generally found to be anti-correlated with the source flux and is typically of the order of hours (see Y. Cavecchi et al. 2025 and references therein for a further discussion). This anti-correlation is also found in a larger sample of NS-LMXBs with type-I X-ray bursts, as can be seen in the trend of the distribution of such systems in the $L_{\text{bol}} - t_{\text{rec}}$ plane, extending from $t_{\text{rec}} \sim 10^8$ s at $L_{\text{bol}} \sim 0.1\%L_{\text{Edd}}$ to $t_{\text{rec}} \sim 10^3$ s at $L_{\text{bol}} \sim 100\%L_{\text{Edd}}$ (see figure 1 in T. Kormpakis et al. 2025). Such a trend is expected, since a higher L_{bol} implies a higher accretion rate, reducing the time needed to accumulate enough amount of matter to trigger thermonuclear runaway. Based on this observed trend, $t_{\text{rec}} \sim 8200$ s as measured for EP J1711–3332 would imply a luminosity of $L_{\text{bol}} \sim 10\%L_{\text{Edd}}$, which is higher by 1–2 orders of magnitude than the luminosity we measured in Section 4.2. We also found an increasing trend for the persistent emission count rate during the *NuSTAR* observation, which is qualitatively consistent with the decreasing trend of t_{rec} (Section 3.1.2). We further note that the increase in the count rate was energy-dependent, i.e., the count rate in the 3–10 keV band rose faster than that in the 10–79 keV band, demonstrating a slow evolution of the spectral shape in real time (Figure 3).

The spectral properties of the persistent emission are typical of a hard spectral state (Section 4.4), which is also the case for several other clocked bursters, including the prototype, GS 1826–24 (e.g. P. Ubertini et al. 1999).

We also estimated the α parameter for bursts No. 5, 6 and 10, which has a high value of 120–130 (Section 3.4.3). As a comparison, GS 1826–24 had an α value of ~ 60 (P. Ubertini et al. 1999). Further assuming that the mass and radius of the NS are $1.4M_{\odot}$ and 11.2 km, we estimated the mean hydrogen mass fraction at igni-

nition to be $\bar{X} \approx 0.09 - 0.11$ (using equation (11) in D. K. Galloway et al. 2022), corresponding to helium-rich burst fuel. Since we expect the accreted gas from the K-type companion to be hydrogen-rich, this implies that most of the accreted hydrogen is consumed by stable burning before a helium burst ignites (burning regime (III) in D. K. Galloway & L. Keek 2021).

5. SUMMARY

We summarize the main results on this new transient NS binary system, EP J1711–3332, as derived from X-ray and optical observations:

- EP J1711–3332 is a clocked burster and its burst recurrence time can be characterized over a subset of nine bursts spanning 1.6 days around the *NuSTAR* observation, which is $t_{\text{rec}} = 8196 \pm 177$ s. A likely linear decrease of its recurrence time ($\dot{t}_{\text{rec}} = -270 \pm 110$ s day $^{-1}$) is also detected, although notable scatter remains. Remarkably, the *NuSTAR* light curve demonstrated an increasing trend, which is qualitatively consistent with the decrease of t_{rec} .
- EP J1711–3332 is an eclipsing binary with an orbital period of $P_{\text{orb}} = 6.48301 \pm 0.00003$ hr and a typical X-ray eclipse duration of $D_{\star,X} = 1245.5_{-6.5}^{+6.9}$ s. Apart from the eclipses, the source also exhibits dip events that seem to occur mostly at the same orbital phase range. The presence of the dips also exhibits a possible correlation with the source flux. The mass and radius of the companion star are estimated to be $M_2 \approx 0.6 - 0.8 M_{\odot}$ and $R_2 \approx 0.7 - 0.8 R_{\odot}$, pointing to a K-type star. The binary inclination is $i \approx 73 - 75$ °.
- Eclipses and dips are also present in the ULTRACAM optical light curves. The optical eclipses are broader and shallower than in X-rays and show a clear wavelength dependence, with longer and less deep eclipses in the redder band. By comparing the optical and X-ray ingress and egress times, we infer that a substantial fraction of the optical emission arises from an extended region in the accretion flow (disk and/or stream impact region). The ULTRACAM data also reveal a short optical flare occurring during the eclipse. The event shows a blueward color change at peak and lacks an X-ray counterpart, pointing to a magnetic flare on the Roche-lobe-filling companion star.
- The distance of the system is constrained to $\sim 2.0 - 6.4$ kpc. With this distance range, the Eddington luminosity ratio of EP J1711–3332 during the *NuSTAR* observation is estimated to be $L_{\text{bol}}/L_{\text{Edd}} \sim 0.2\% - 1.6\%$.
- During the first 21 days of the outburst, the persistent emission of EP J1711–3332 showed moder-

ate variation in the observed flux, but the spectral shape did not show significant changes. The spectral properties are typical of a hard spectral state.

- The ratio of accretion energy to thermonuclear energy (α) is estimated to be 120–130, which corresponds to a mean hydrogen mass fraction at ignition of $\bar{X} \approx 0.09 - 0.11$, implying helium bursts with the accreted hydrogen being depleted by stable burning in-between bursts.

ACKNOWLEDGMENTS

This work is based on the data obtained with the *Einstein Probe*, a space mission led by the Chinese Academy of Sciences, in collaboration with the European Space Agency, the Max Planck Institute for Extraterrestrial Physics (Germany), and the Centre National d’Études Spatiales (France). This work is supported by the National Natural Science Foundation of China (Grant Nos. 12333004 and 12433005), and the Strategic Priority Research Program of the Chinese Academy of Sciences (Grant No. XDB0550200). This work is also based on the data obtained with: the *NuSTAR* mission, a project led by the California Institute of Technology, managed by the Jet Propulsion Laboratory, and funded by NASA; and ULTRACAM on the 3.5-m NTT at La Silla, Chile. YLW is supported by the China Scholarship Council (No. 202404910397). AM and NR are supported by the European Research Council (ERC) under the European Union’s Horizon Europe research and innovation programme (ERC Consolidator Grant “MAGNESIA” No. 817661, and ERC Proof of Concept “DeepSpacePULSE” No. 101189496; PI: NR). FCZ is supported by a Ramón y Cajal fellowship (grant agreement RYC2021-030888-I). EP is supported by a Juan de la Cierva fellowship (JDC2022-049957-I). YLW, FCZ, EP, AM and NR are also supported by the Spanish grant PID2023-153099NA-I00 (PI: FCZ) and Unidad de Excelencia María de Maeztu CEX2020-001058-M. VSD and ULTRACAM are supported by STFC grant ST/Z000033/1. JB-P and IR acknowledge financial support from Spanish grants PID2021-125627OB-C31 and PID2024-158486OB-C31 funded by MCIU/AEI/10.13039/501100011033 and by “ERDF A way of making Europe”, by the Generalitat de Catalunya/CERCA programme, and by the European Research Council (ERC) under the European Union’s Horizon Europe programme (ERC Advanced Grant SPOTLESS; no. 101140786). JB-P acknowledges support from Spanish grant PRE2022-101942. AP acknowledges support from grants PID2024-155316NB-I00, PID2021-124581OB-I0, and 2021SGR00426. YC acknowledges support from the grant RYC2021-032718-I, financed by MCIN/AEI/10.13039/501100011033 and the European Union NextGenerationEU/PRTR. This

Table A1. Journal of the X-ray observations of EP J1711–3332 presented in this work

Telescope	Mode	ObsID	Start – End Time (UTC) (YYYY-MM-DD HH:MM:SS)	Exposure (ks)
EP/FXT	FF+FF	06800000695	2025-06-25 14:09:08 – 2025-06-25 15:00:09	3.1
EP/FXT	PW+TM	06800000697	2025-06-26 14:08:34 – 2025-06-26 16:35:19	6.0
EP/FXT	PW+TM	06800000702	2025-06-27 06:08:10 – 2025-06-27 06:18:35	0.6
EP/FXT	PW+TM	06800000698	2025-06-27 10:56:04 – 2025-06-27 13:22:38	6.1
EP/FXT	FF+FF	06800000705	2025-06-27 18:55:52 – 2025-06-27 21:22:22	4.8
<i>NuSTAR</i>	–	81101345002	2025-06-27 20:50:57 – 2025-06-28 21:14:06	46.7
EP/FXT	FF+FF	06800000706	2025-06-28 01:19:42 – 2025-06-28 03:46:09	3.1
EP/FXT	PW+TM	06800000699	2025-06-28 10:55:28 – 2025-06-28 13:22:06	6.1
EP/FXT	FF+FF	06800000707	2025-06-28 17:19:19 – 2025-06-28 18:09:41	3.0
EP/FXT	FF+FF	06800000708	2025-06-29 01:19:07 – 2025-06-29 03:45:22	3.3
EP/FXT	PW+TM	06800000700	2025-06-29 09:18:55 – 2025-06-29 11:45:22	6.1
EP/FXT	PW+TM	06800000701	2025-06-30 17:18:07 – 2025-06-30 19:44:17	5.1
EP/FXT	PW+TM	06800000717	2025-07-01 15:41:30 – 2025-07-01 18:07:31	6.0
EP/FXT	PW+TM	06800000718	2025-07-02 06:05:06 – 2025-07-02 08:31:01	5.2
EP/FXT	PW+TM	06800000720	2025-07-03 14:04:08 – 2025-07-03 16:29:54	6.0
EP/FXT	PW+TM	06800000722	2025-07-05 09:14:35 – 2025-07-05 11:40:20	6.0
EP/FXT	PW+TM	06800000723	2025-07-06 10:50:04 – 2025-07-06 13:15:25	6.0
EP/FXT	PW+TM	06800000724	2025-07-07 12:24:40 – 2025-07-07 14:50:28	6.0
EP/FXT	PW+TM	11900302977	2025-07-09 05:59:06 – 2025-07-09 08:24:56	6.0
EP/FXT	PW+TM	11900304129	2025-07-10 08:16:45 – 2025-07-10 11:25:05	5.8
EP/FXT	PW+TM	11900305153	2025-07-11 11:03:37 – 2025-07-11 13:11:02	4.9
EP/FXT	PW+TM	11900306945	2025-07-12 13:01:38 – 2025-07-12 16:13:15	5.6
EP/FXT	PW+TM	11900307969	2025-07-13 15:49:35 – 2025-07-13 17:57:19	4.3

NOTE—FF: Full Frame mode; PW: Partial Window mode; TM: Timing mode. PW+TM denotes the configuration in which FXT-A and FXT-B are set in PW and TM, respectively.

work received financial support from INAF through the GRAWITA 2022 Large Program Grant.

Facilities: *Einstein Probe* (WXT and FXT), *NuSTAR*, ESO-NTT (ULTRACAM).

Software: FXTDAS v1.20 (H.-S. Zhao et al. 2025), HEASOFT v6.35.2 (Nasa High Energy Astrophysics Science Archive Research Center (Heasarc) 2014), Matplotlib v3.10 (J. D. Hunter 2007), PINT (J. Luo et al. 2021), XSPEC v12.15.0 (K. A. Arnaud 1996), NuSTAR-DAS v2.1.4a.

APPENDIX

In this appendix, we present supplementary tables and figures to complement the results reported in the main text. The details of the X-ray observations presented in this work are listed in Table A1. The properties of the 16 detected type-I X-ray bursts are listed in Table A2. The light curves and spectra collected by EP/FXT are respectively presented in Figure A1 and Figure A2. The results of the time-averaged spectral analyses for the bursts detected by *NuSTAR* and EP/FXT are shown in Figure A3 and Figure A4, respectively. The results of the time-resolved spectral analyses for the bursts detected by *NuSTAR* and EP/FXT are shown in Figure A5 and Figure A6, respectively. Burst No. 8 is

the only burst simultaneously covered by both EP/FXT and *NuSTAR*, and its spectral analysis results are presented separately in Figure A7.

Table A2. Properties of the detected bursts. The detection significance in the fourth column represents the Poisson tail probability converted to a Gaussian-equivalent significance, expressed in units of σ (see Section 3.1.1). The date (UTC) and epoch (TDB; i.e., barycentric dynamical time) correspond to the burst times of arrival (TOAs; see Section 3.1.2). The width is defined as the duration between the burst start and end times, and the fluence is the total number of photons detected within the burst duration. The last column, t_{rec} , is the burst recurrence time (see Section 3.1.2), defined as the time elapsed between the start of the burst and the start of the previous burst. Associated 1σ uncertainties are indicated in parentheses on the last digit.

Burst No.	Telescope	ObsID	Significance	Start Epoch (σ)	Start Date (YYYY-MM-DD)	Start Time (HH:MM:SS)	Peak Time (HH:MM:SS)	Width (s)	Fluence (counts)	t_{rec} (s)
1	EP/FXT	06800000695	6.1	60851.605451	2025-06-25	14:30:41	14:30:58	144	988(3)	—
2	EP/FXT	06800000697	5.7	60852.601970	2025-06-26	14:25:40	14:25:57	117	959(5)	—
3	EP/FXT	06800000705	4.2	60853.808807	2025-06-27	19:23:31	19:23:42	101	796(5)	—
4	<i>NuSTAR</i>	81101345002	8.1	60853.906121	2025-06-27	21:43:39	21:43:48	43	826(6)	8408(47)
5	<i>NuSTAR</i>	81101345002	9.0	60854.001211	2025-06-28	00:00:35	00:00:40	105	1549(7)	8216(41)
6	<i>NuSTAR</i>	81101345002	7.9	60854.097852	2025-06-28	02:19:45	02:19:58	141	1724(3)	8350(59)
7	<i>NuSTAR</i>	81101345002	10.1	60854.291929	2025-06-28	06:59:13	06:59:30	118	1688(8)	8384(60)
8	<i>NuSTAR</i>	81101345002	9.9	60854.481011	2025-06-28	11:31:30	11:31:47	141	1939(4)	8168(59)
8	EP/FXT	06800000699	6.9	60854.481203	2025-06-28	11:31:46	11:31:57	75	1190(6)	8168(59)
9	<i>NuSTAR</i>	81101345002	10.1	60854.666920	2025-06-28	15:59:12	15:59:23	123	1824(11)	8031(59)
10	<i>NuSTAR</i>	81101345002	8.1	60854.760495	2025-06-28	18:13:57	18:14:08	123	1739(8)	8085(54)
11	EP/FXT	06800000700	5.5	60855.413211	2025-06-29	09:53:52	09:53:59	73	1255(10)	8056(51)
12	EP/FXT	06800000718	6.9	60858.268541	2025-07-02	06:25:32	06:25:45	81	1559(8)	—
13	EP/FXT	06800000720	5.9	60859.675801	2025-07-03	16:11:59	16:12:14	115	2066(9)	—
14	EP/FXT	06800000724	7.4	60863.584668	2025-07-07	14:00:46	14:00:55	103	2227(12)	—
15	EP/FXT	11900304129	9.3	60866.458318	2025-07-10	10:58:49	10:59:14	113	2043(6)	—
16	EP/FXT	11900305153	10.2	60867.464511	2025-07-11	11:07:44	11:08:01	141	2313(7)	—

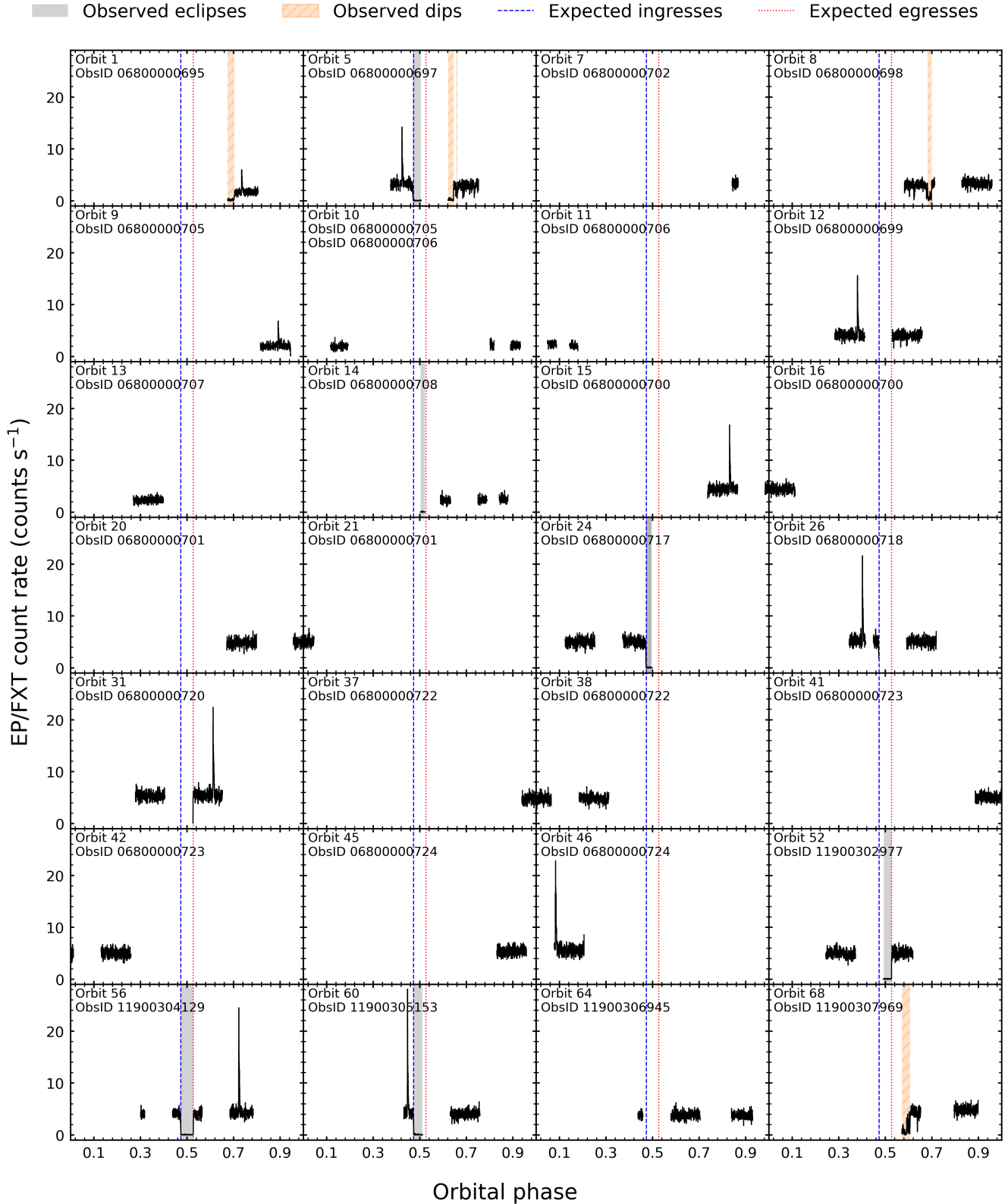


Figure A1. Phase-resolved light curves of all 22 EP/FXT observations presented in this work. Each panel shows the data obtained in one orbit of the binary system. The orbit observed by the first FXT observation is defined as Orbit 1. The expected ingress (dashed blue lines) and egress (dotted red lines) epochs are calculated from ObsID 11900304129. The shaded gray areas are the observed eclipse periods. The orange hatched bands are the observed dips. Only the data collected by FXT-A are shown.

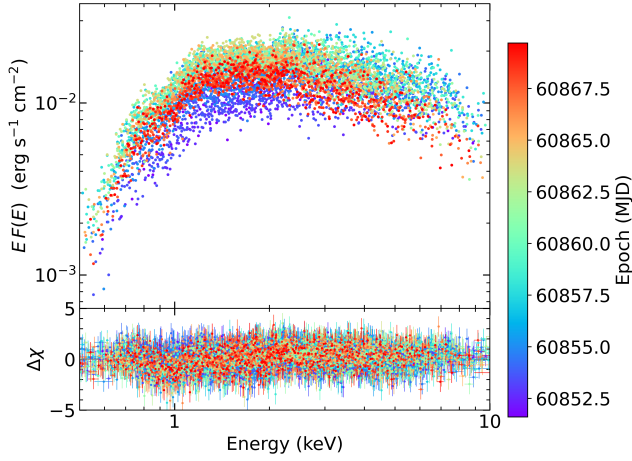


Figure A2. Evolution of the unfolded spectra of EP J1711–3332 as observed by EP/FXT (upper panel) and the spectral fitting residuals (lower panel). The model adopted for spectral analysis is `TBabs × (thComp × bbodyrad + diskbb)`. For clarity, only data collected by FXT-A are shown and error bars of the data are omitted in the upper panel.

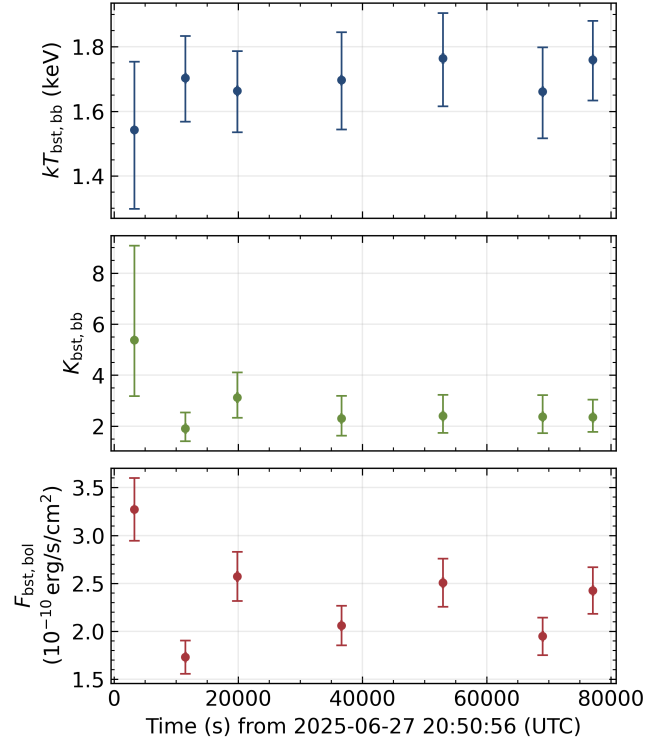


Figure A3. Results of the time-averaged spectral analysis for the seven type-I X-ray bursts detected by *NuSTAR*. The `Xspec` model adopted in the analysis is `TBabs × (nthComp + bbodyrad)`. $T_{\text{bst,bb}}$ and $K_{\text{bst,bb}}$ are the temperature and normalization of the `bbodyrad` component, which represents the burst emission. $F_{\text{bst,bol}}$ is the averaged unabsorbed bolometric flux of the burst emission, which is approximated by the flux of the `bbodyrad` component, after extrapolating it to the 0.01–100 keV band. The uncertainties for $kT_{\text{bst,bb}}$ and $K_{\text{bst,bb}}$ are at 90% confidence level. For $F_{\text{bst,bol}}$, we adopted a nominal uncertainty of 10% of its value.

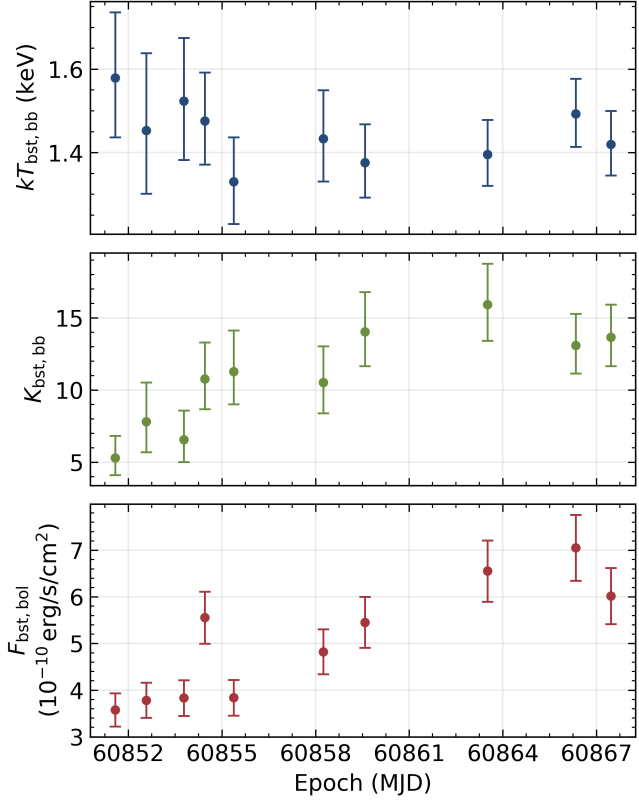


Figure A4. Results of the time-averaged spectral analysis for the ten type-I X-ray bursts detected by EP/FXT. The `Xspec` model adopted in the analysis is `TBabs × bbodyrad`. $T_{\text{bst,bb}}$ and $K_{\text{bst,bb}}$ are the temperature and normalization of the `bbodyrad` component, which represents the burst emission. $F_{\text{bst,bol}}$ is the averaged unabsorbed bolometric flux of the burst emission, which is approximated by the flux of the `bbodyrad` component, after extrapolating it to the 0.01–100 keV band. The uncertainties for $kT_{\text{bst,bb}}$ and $K_{\text{bst,bb}}$ are at 90% confidence level. For $F_{\text{bst,bol}}$, we adopted a nominal uncertainty of 10% of its value.

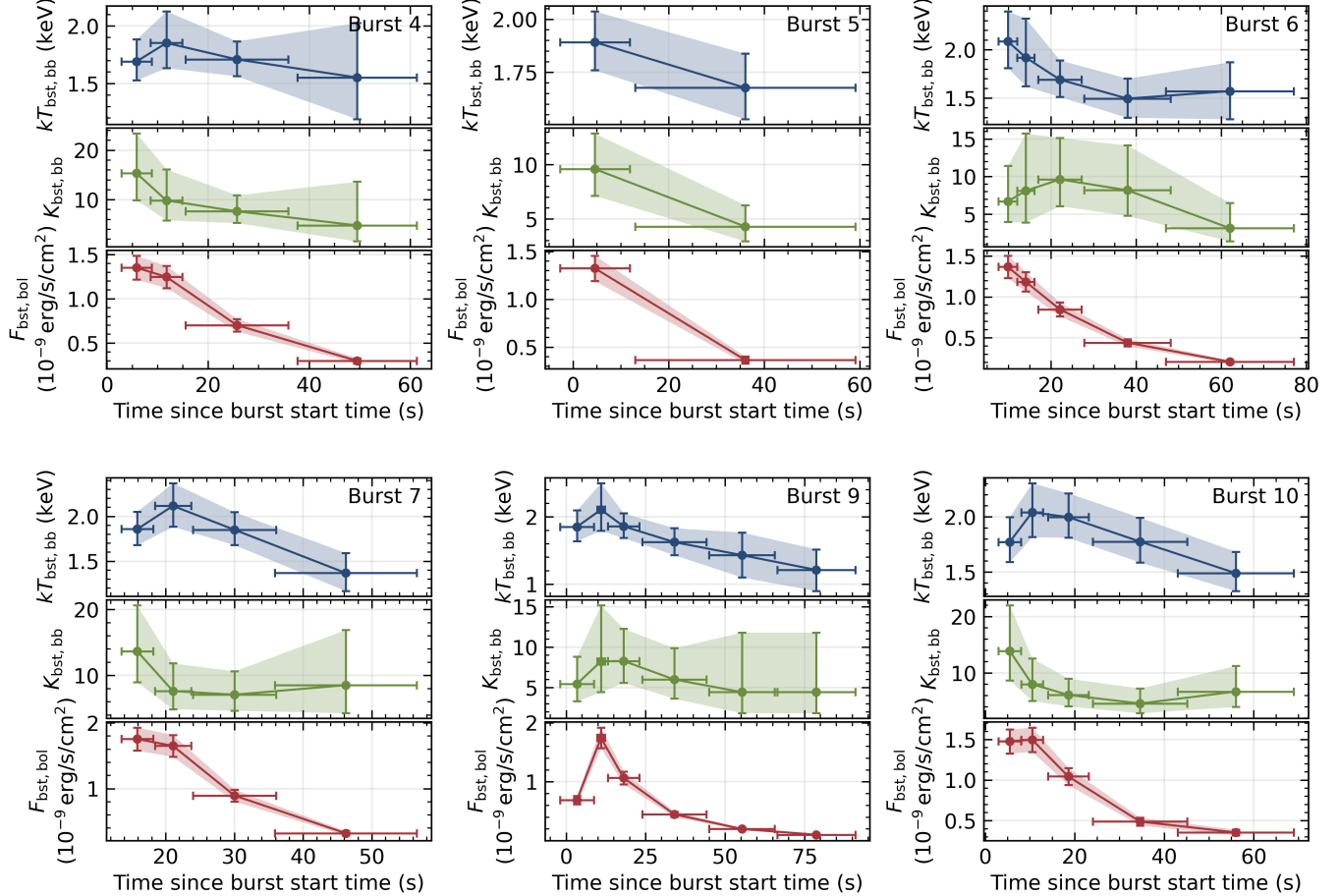


Figure A5. Evolution of key spectral parameters obtained from the time-resolved spectral analysis for six out of seven type-I X-ray bursts detected by *NuSTAR*. Results for burst No. 8 are presented in Figure A7. The `Xspec` model adopted in the analysis is `TBabs × (nthComp + bbodyrad)`. $T_{\text{bst,bb}}$ and $K_{\text{bst,bb}}$ are the temperature and normalization of the `bbodyrad` component, which models the burst emission. $F_{\text{bst,bol}}$ is the unabsorbed bolometric flux of the burst emission, which is approximated by the flux of the `bbodyrad` component, after extrapolating it to the 0.01–100 keV band. The values of $K_{\text{bst,bb}}$ were linked for the last two time segments in burst No. 9 during spectral fitting, because they are otherwise unconstrained. Shaded areas denote uncertainties at 90% confidence level for $kT_{\text{bst,bb}}$ and $K_{\text{bst,bb}}$. For $F_{\text{bst,bol}}$, we adopted a nominal uncertainty of 10% of its value.

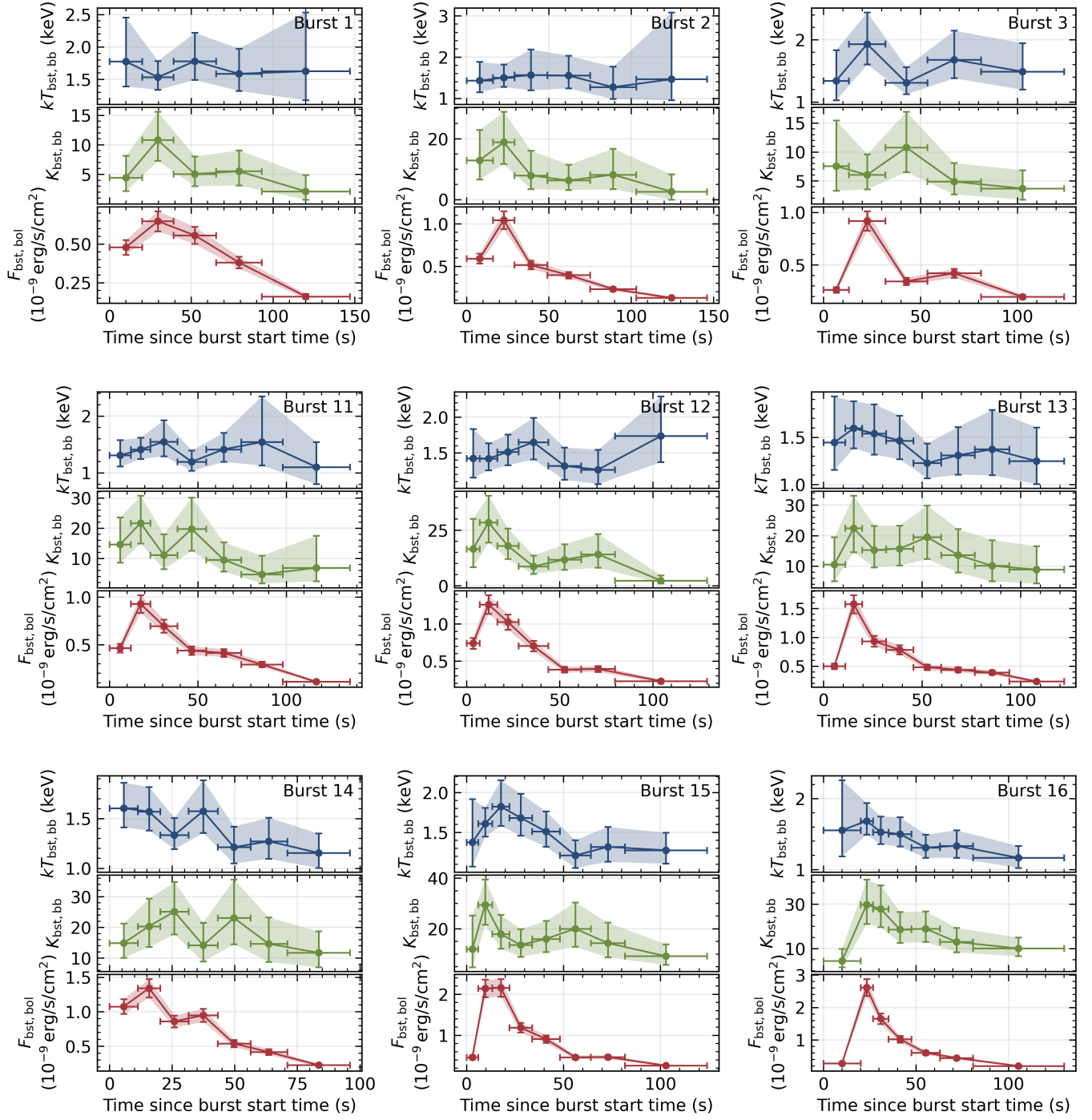


Figure A6. Evolution of key spectral parameters obtained from the time-resolved spectral analysis for nine out of ten type-I X-ray bursts detected by EP/FXT. Results for burst No. 8 are presented in Figure A7. The Xspec model adopted in the analysis is $T\text{Babs} \times \text{bbodyrad}$. $T_{bst,bb}$ and $K_{bst,bb}$ are the temperature and normalization of the bbodyrad component, which models the burst emission. $F_{bst,bol}$ is the unabsorbed bolometric flux of the burst emission, which is approximated by the flux of the bbodyrad component, after extrapolating it to the 0.01–100 keV band. Shaded areas denote uncertainties at 90% confidence level for $kT_{bst,bb}$ and $K_{bst,bb}$. For $F_{bst,bol}$, we adopted a nominal uncertainty of 10% of its value.

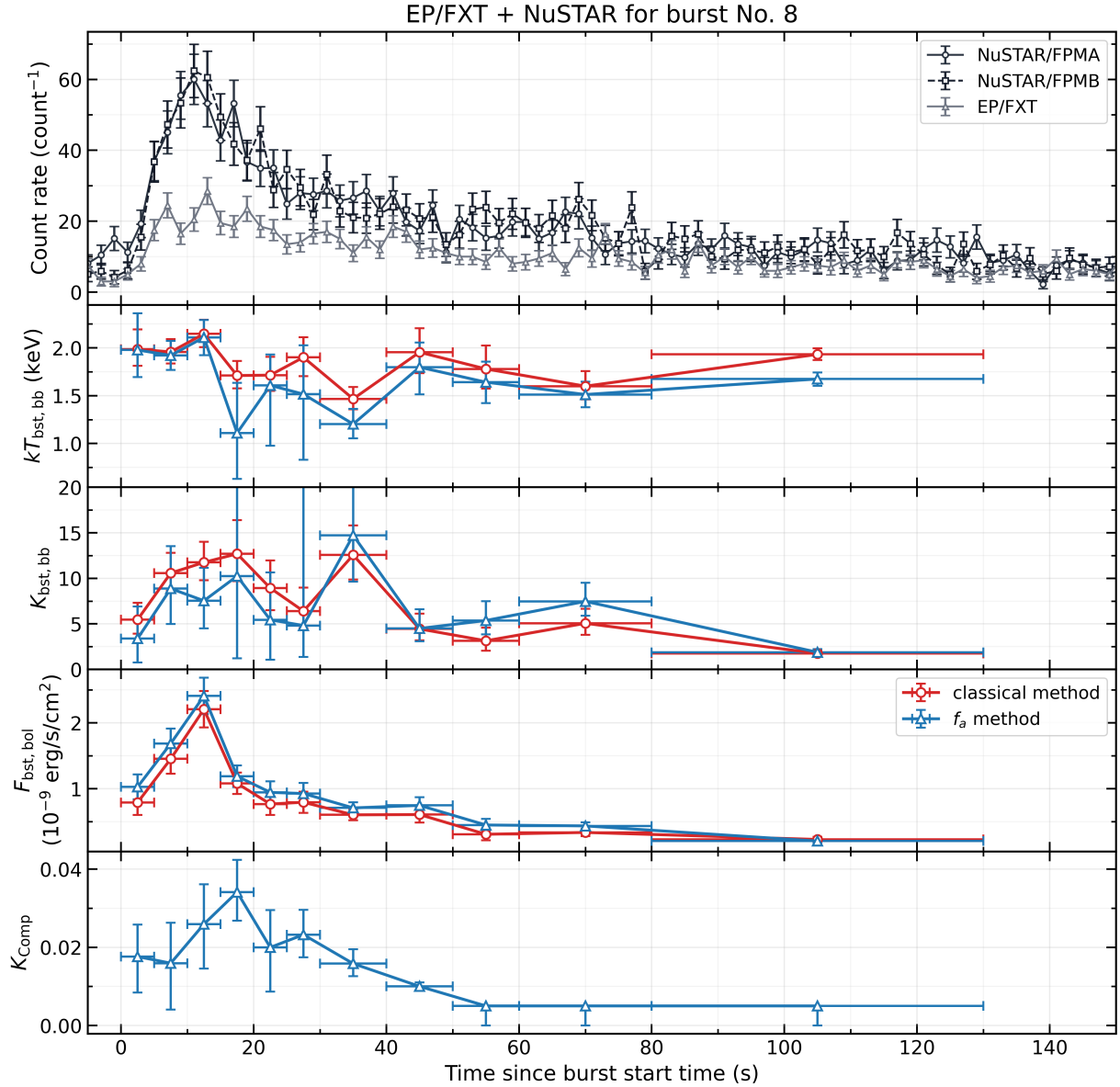


Figure A7. Comparison of the results obtained with the two spectral fitting methods for burst No. 8 observed simultaneously by EP/FXT and *NuSTAR*. From top to bottom, the panels show: the 2-s bin light curves from EP/FXT (0.5–10 keV; gray) and *NuSTAR* (3–50 keV; black); the blackbody temperature ($kT_{\text{bst,bb}}$); the blackbody normalization ($K_{\text{bst,bb}}$); the bolometric flux ($F_{\text{bst,bol}}$; in units of $10^{-9} \text{ erg/s/cm}^{-2}$); and the normalization of the `nthComp` component (K_{Comp}). Red circles denote results obtained with the classical method, while blue triangles correspond to the f_a method.

REFERENCES

- Andersen, B. C., & Ransom, S. M. 2018, *ApJL*, 863, L13, doi: [10.3847/2041-8213/aad59f](https://doi.org/10.3847/2041-8213/aad59f)
- Aranzana, E., Sánchez-Fernández, C., & Kuulkers, E. 2016, *A&A*, 586, A142, doi: [10.1051/0004-6361/201526816](https://doi.org/10.1051/0004-6361/201526816)
- Arnaud, K. A. 1996, in *Astronomical Society of the Pacific Conference Series*, Vol. 101, *Astronomical Data Analysis Software and Systems V*, ed. G. H. Jacoby & J. Barnes, 17
- Bahramian, A., & Degenaar, N. 2022, *Low-Mass X-ray Binaries*, ed. C. Bambi & A. Santangelo (Singapore: Springer Nature Singapore), 1–62, doi: [10.1007/978-981-16-4544-0_94-1](https://doi.org/10.1007/978-981-16-4544-0_94-1)
- Bult, P., Altamirano, D., Arzoumanian, Z., et al. 2022, *ApJL*, 935, L32, doi: [10.3847/2041-8213/ac87f9](https://doi.org/10.3847/2041-8213/ac87f9)
- Cavecchi, Y., Galloway, D., Heger, A., et al. 2025, arXiv e-prints, arXiv:2506.11966, doi: [10.48550/arXiv.2506.11966](https://doi.org/10.48550/arXiv.2506.11966)
- Chakraborty, M., Bhattacharyya, S., & Mukherjee, A. 2011, *MNRAS*, 418, 490, doi: [10.1111/j.1365-2966.2011.19499.x](https://doi.org/10.1111/j.1365-2966.2011.19499.x)
- Cornelisse, R., in't Zand, J. J. M., Verbunt, F., et al. 2003, *A&A*, 405, 1033, doi: [10.1051/0004-6361:20030629](https://doi.org/10.1051/0004-6361:20030629)
- Cowie, F. J., Hughes, A. K., Fender, R. P., & collaboration, S. M. X.-K. 2025, *The Astronomer's Telegram*, 17258, 1
- Demircan, O., & Kahraman, G. 1991, *Ap&SS*, 181, 313, doi: [10.1007/BF00639097](https://doi.org/10.1007/BF00639097)
- Dhillon, V. S., Marsh, T. R., Stevenson, M. J., et al. 2007, *MNRAS*, 378, 825, doi: [10.1111/j.1365-2966.2007.11881.x](https://doi.org/10.1111/j.1365-2966.2007.11881.x)
- Dhillon, V. S., Bezwada, N., Black, M., et al. 2021, *MNRAS*, 507, 350, doi: [10.1093/mnras/stab2130](https://doi.org/10.1093/mnras/stab2130)
- Di Salvo, T., Papitto, A., Marino, A., Iaria, R., & Burderi, L. 2023, in *Handbook of X-ray and Gamma-ray Astrophysics*, 147, doi: [10.1007/978-981-16-4544-0_103-1](https://doi.org/10.1007/978-981-16-4544-0_103-1)
- Dohi, A., Nishimura, N., Hirai, R., et al. 2025, *PASJ*, 77, L17, doi: [10.1093/pasj/psaee117](https://doi.org/10.1093/pasj/psaee117)
- Doroshenko, V. 2024, arXiv e-prints, arXiv:2403.03127, doi: [10.48550/arXiv.2403.03127](https://doi.org/10.48550/arXiv.2403.03127)
- Edenhofer, G., Zucker, C., Frank, P., et al. 2024, *A&A*, 685, A82, doi: [10.1051/0004-6361/202347628](https://doi.org/10.1051/0004-6361/202347628)
- Eggleton, P. P. 1983, *ApJ*, 268, 368, doi: [10.1086/160960](https://doi.org/10.1086/160960)
- Fiocchi, M., Bazzano, A., Bruni, G., et al. 2019, *ApJ*, 887, 30, doi: [10.3847/1538-4357/ab4d59](https://doi.org/10.3847/1538-4357/ab4d59)
- Galloway, D. K., Johnston, Z., Goodwin, A., & He, C.-C. 2022, *ApJS*, 263, 30, doi: [10.3847/1538-4365/ac98c9](https://doi.org/10.3847/1538-4365/ac98c9)
- Galloway, D. K., & Keek, L. 2021, in *Astrophysics and Space Science Library*, Vol. 461, *Timing Neutron Stars: Pulsations, Oscillations and Explosions*, ed. T. M. Belloni, M. Méndez, & C. Zhang, 209–262, doi: [10.1007/978-3-662-62110-3_5](https://doi.org/10.1007/978-3-662-62110-3_5)
- Galloway, D. K., in't Zand, J., Chenevez, J., et al. 2020, *ApJS*, 249, 32, doi: [10.3847/1538-4365/ab9f2e](https://doi.org/10.3847/1538-4365/ab9f2e)
- García, J., Dauser, T., Lohfink, A., et al. 2014, *ApJ*, 782, 76, doi: [10.1088/0004-637X/782/2/76](https://doi.org/10.1088/0004-637X/782/2/76)
- Gordon, K. 2024, *The Journal of Open Source Software*, 9, 7023, doi: [10.21105/joss.07023](https://doi.org/10.21105/joss.07023)
- Gordon, K. D., Clayton, G. C., Decler, M., et al. 2023, *ApJ*, 950, 86, doi: [10.3847/1538-4357/accb59](https://doi.org/10.3847/1538-4357/accb59)
- Guillot, S., Xin, L., Marino, A., Coti Zelati, F., & Rea, N. 2025, *The Astronomer's Telegram*, 17272, 1
- Harrison, F. A., Craig, W. W., Christensen, F. E., et al. 2013, *ApJ*, 770, 103, doi: [10.1088/0004-637X/770/2/103](https://doi.org/10.1088/0004-637X/770/2/103)
- Hastings, W. K. 1970, *Biometrika*, 57, 97, doi: [10.1093/biomet/57.1.97](https://doi.org/10.1093/biomet/57.1.97)
- Hunter, J. D. 2007, *Computing in Science and Engineering*, 9, 90, doi: [10.1109/MCSE.2007.55](https://doi.org/10.1109/MCSE.2007.55)
- Illiano, G., Papitto, A., Marino, A., et al. 2024, *A&A*, 691, A189, doi: [10.1051/0004-6361/202451703](https://doi.org/10.1051/0004-6361/202451703)
- Jordi, K., Grebel, E. K., & Ammon, K. 2006, *A&A*, 460, 339, doi: [10.1051/0004-6361:20066082](https://doi.org/10.1051/0004-6361:20066082)
- Joss, P. C., & Rappaport, S. A. 1984, *ARA&A*, 22, 537, doi: [10.1146/annurev.aa.22.090184.002541](https://doi.org/10.1146/annurev.aa.22.090184.002541)
- Kaastra, J. S., & Bleeker, J. A. M. 2016, *A&A*, 587, A151, doi: [10.1051/0004-6361/201527395](https://doi.org/10.1051/0004-6361/201527395)
- Kajava, J. J. E., Motta, S. E., Sanna, A., et al. 2019, *MNRAS*, 488, L18, doi: [10.1093/mnrasl/slz089](https://doi.org/10.1093/mnrasl/slz089)
- Kong, A. K. H., Aryan, A., Li, K. L., et al. 2025, *The Astronomer's Telegram*, 17280, 1
- Kormpakis, T., Linares, M., & José, J. 2025, *MNRAS*, 540, 2305, doi: [10.1093/mnras/staf853](https://doi.org/10.1093/mnras/staf853)
- Kuulkers, E., Kouveliotou, C., Belloni, T., et al. 2013, *A&A*, 552, A32, doi: [10.1051/0004-6361/201219447](https://doi.org/10.1051/0004-6361/201219447)
- La Monaca, F., Di Marco, A., Coti Zelati, F., et al. 2025, *A&A*, 702, A101, doi: [10.1051/0004-6361/202555134](https://doi.org/10.1051/0004-6361/202555134)
- Lewin, W. H. G., van Paradijs, J., & Taam, R. E. 1993, *SSRv*, 62, 223, doi: [10.1007/BF00196124](https://doi.org/10.1007/BF00196124)
- Ludlam, R. M. 2024, *Ap&SS*, 369, 16, doi: [10.1007/s10509-024-04281-y](https://doi.org/10.1007/s10509-024-04281-y)
- Luo, J., Ransom, S., Demorest, P., et al. 2021, *ApJ*, 911, 45, doi: [10.3847/1538-4357/abe62f](https://doi.org/10.3847/1538-4357/abe62f)
- Malacaria, C., Papitto, A., Campana, S., et al. 2025, *A&A*, 699, A288, doi: [10.1051/0004-6361/202554075](https://doi.org/10.1051/0004-6361/202554075)
- Marino, A., Del Santo, M., Cocchi, M., et al. 2019, *MNRAS*, 490, 2300, doi: [10.1093/mnras/stz2726](https://doi.org/10.1093/mnras/stz2726)
- Marino, A., Anitra, A., Mazzola, S. M., et al. 2022, *MNRAS*, 515, 3838, doi: [10.1093/mnras/stac2038](https://doi.org/10.1093/mnras/stac2038)
- Marino, A., Coti Zelati, F., Wang, Y. L., et al. 2025, *The Astronomer's Telegram*, 17271, 1

- McAllister, M., Littlefair, S. P., Parsons, S. G., et al. 2019, MNRAS, 486, 5535, doi: [10.1093/mnras/stz976](https://doi.org/10.1093/mnras/stz976)
- Molkov, S. V., Lutovinov, A. A., Tsygankov, S. S., et al. 2024, A&A, 690, A353, doi: [10.1051/0004-6361/202450581](https://doi.org/10.1051/0004-6361/202450581)
- Motta, S., D'Aì, A., Papitto, A., et al. 2011, MNRAS, 414, 1508, doi: [10.1111/j.1365-2966.2011.18483.x](https://doi.org/10.1111/j.1365-2966.2011.18483.x)
- Nasa High Energy Astrophysics Science Archive Research Center (Heasarc). 2014, HEAsoft: Unified Release of FTOOLS and XANADU,, Astrophysics Source Code Library, record ascl:1408.004
- Ng, M., Ray, P. S., Sanna, A., et al. 2024, ApJL, 968, L7, doi: [10.3847/2041-8213/ad4edb](https://doi.org/10.3847/2041-8213/ad4edb)
- Ni, K. R., Wu, J. H., Wen, W. F., & Yuan, W. 2025, The Astronomer's Telegram, 17247, 1
- Onken, C. A., Wolf, C., Bessell, M. S., et al. 2024, PASA, 41, e061, doi: [10.1017/pasa.2024.53](https://doi.org/10.1017/pasa.2024.53)
- Papitto, A., Di Marco, A., Poutanen, J., et al. 2025, A&A, 694, A37, doi: [10.1051/0004-6361/202451775](https://doi.org/10.1051/0004-6361/202451775)
- Pecaut, M. J., & Mamajek, E. E. 2013, ApJS, 208, 9, doi: [10.1088/0067-0049/208/1/9](https://doi.org/10.1088/0067-0049/208/1/9)
- Pintore, F., Sanna, A., Riggio, A., et al. 2018, MNRAS, 479, 4084, doi: [10.1093/mnras/sty1735](https://doi.org/10.1093/mnras/sty1735)
- Planck Collaboration, Aghanim, N., Ashdown, M., et al. 2016, A&A, 596, A109, doi: [10.1051/0004-6361/201629022](https://doi.org/10.1051/0004-6361/201629022)
- Ransom, S. 2011, PRESTO: Pulsar Exploration and Search TOOlkit,, Astrophysics Source Code Library, record ascl:1107.017 <http://ascl.net/1107.017>
- Ransom, S. M. 2001, PhD thesis, Harvard University, Massachusetts
- Ransom, S. M., Eikenberry, S. S., & Middleditch, J. 2002, AJ, 124, 1788, doi: [10.1086/342285](https://doi.org/10.1086/342285)
- Scargle, J. D., Norris, J. P., Jackson, B., & Chiang, J. 2013, ApJ, 764, 167, doi: [10.1088/0004-637X/764/2/167](https://doi.org/10.1088/0004-637X/764/2/167)
- Smith, D. A., & Dhillon, V. S. 1998, MNRAS, 301, 767, doi: [10.1046/j.1365-8711.1998.02065.x](https://doi.org/10.1046/j.1365-8711.1998.02065.x)
- Susobhanan, A., Kaplan, D. L., Archibald, A. M., et al. 2024, ApJ, 971, 150, doi: [10.3847/1538-4357/ad59f7](https://doi.org/10.3847/1538-4357/ad59f7)
- Ubertini, P., Bazzano, A., Cocchi, M., et al. 1999, ApJL, 514, L27, doi: [10.1086/311933](https://doi.org/10.1086/311933)
- Verner, D. A., Ferland, G. J., Korista, K. T., & Yakovlev, D. G. 1996, ApJ, 465, 487, doi: [10.1086/177435](https://doi.org/10.1086/177435)
- Wang, P. J., Chen, Y. P., Ji, L., et al. 2024, A&A, 689, A47, doi: [10.1051/0004-6361/202348352](https://doi.org/10.1051/0004-6361/202348352)
- Wilms, J., Allen, A., & McCray, R. 2000, ApJ, 542, 914, doi: [10.1086/317016](https://doi.org/10.1086/317016)
- Worpel, H., Galloway, D. K., & Price, D. J. 2013, ApJ, 772, 94, doi: [10.1088/0004-637X/772/2/94](https://doi.org/10.1088/0004-637X/772/2/94)
- Wu, J., Ni, K. R., Wen, W. F., et al. 2025, The Astronomer's Telegram, 17255, 1
- Yang, Z., Zhang, L., Meng, G., et al. 2023, A&A, 669, A15, doi: [10.1051/0004-6361/202142710](https://doi.org/10.1051/0004-6361/202142710)
- Yao, J. M., Manchester, R. N., & Wang, N. 2017, ApJ, 835, 29, doi: [10.3847/1538-4357/835/1/29](https://doi.org/10.3847/1538-4357/835/1/29)
- Yuan, W., Zhang, C., Chen, Y., & Ling, Z. 2022, in Handbook of X-ray and Gamma-ray Astrophysics, 86, doi: [10.1007/978-981-16-4544-0_151-1](https://doi.org/10.1007/978-981-16-4544-0_151-1)
- Yuan, W., Dai, L., Feng, H., et al. 2025, Science China Physics, Mechanics, and Astronomy, 68, 239501, doi: [10.1007/s11433-024-2600-3](https://doi.org/10.1007/s11433-024-2600-3)
- Zdziarski, A. A., Szanecki, M., Poutanen, J., Gierliński, M., & Biernacki, P. 2020, MNRAS, 492, 5234, doi: [10.1093/mnras/staa159](https://doi.org/10.1093/mnras/staa159)
- Zhao, H.-S., Li, C.-K., Wang, J., et al. 2025, Radiation Detection Technology and Methods, 9, 215, doi: [10.1007/s41605-025-00526-8](https://doi.org/10.1007/s41605-025-00526-8)